공학석사학위논문

고속 슈라우드 원심압축기 안정성에 대한 편심 영향 측정

Measurement of Eccentricity Effects on Stability of a High-Speed Shrouded Centrifugal Compressor

2017년 8월

서울대학교 대학원

기계항공공학부

김 수 용

고속 슈라우드 원심압축기 안정성에 대한 편심 영향 측정

Measurement of Eccentricity Effects on Stability of a High-Speed Shrouded Centrifugal Compressor

지도교수 송 성 진

이 논문을 공학석사 학위논문으로 제출함

2017년 4월

서울대학교 대학원

기계항공공학부

김 수 용

김수용의 공학석사 학위논문을 인준함

2017년 6월

위 원 장 _____

부위원장 _____

위 원 _____

Abstract

Measurement of Eccentricity Effects on Stability of a High-Speed Shrouded Centrifugal Compressor

Suyong Kim
Department of Mechanical and Aerospace Engineering
The Graduate School
Seoul National University

Eccentricity effects on stability has been experimentally measured with a high-speed shrouded centrifugal compressor in Korea Aerospace Research Institute. The research examines influences of eccentricity on the onset of rotating stall and surge, the types and the behavior of instabilities.

For the experiments, a test section of a turbocharger test rig has been re-designed and manufactured; then, eccentricity can be adjusted by moving casings with highly accurate shims rather than moving a rotor shaft. In the test section, fast response pressure sensors (Kulite sensors) and gap sensors have been installed to measure unsteady flow and to monitor the relative center position between the rotor shaft and the casing. Totally thirty two Kulite sensors have been used and circumferentially located eight Kulite sensors have measured rotating stall. Those

four sets of Kulite sensors have been located at impeller inlet, diffuser inlet, seal inlet, and seal gland to figure out where instability arises and to understand the behavior of instabilities—rotating stall and surge. Static pressures, total pressures, and total temperatures have been also measured to obtain steady performance—pressure rise coefficient.

Experiments have been conducted at five levels of eccentricity. Baseline is 9.6% eccentricity and this case has been treated as concentric condition. The other four eccentricities are 19.6%, 26.2%, 37.8%, and 58.7%. All experiments have been operated at the design speed of 40,000 rpm.

Experimental results present that: (1) the compressor directly goes into classic surge at the baseline case. (2) the compressor has two cells of rotating stall and stall cells rotate at the rate of 0.19 times rotor frequency at the baseline case. (3) overall pressure rise coefficient through the compressor has little influenced by eccentricity but pressure rise coefficient through the impeller has been degraded as eccentricity increases due to larger leakage along the secondary passage. (4) stalling flow coefficient is sensitive to eccentricity but the onset of surge is not sensitive to eccentricity; consequently, rotating stall precedes classic surge at larger flow coefficient as eccentricity increases.

Keyword : Eccentricity; Centrifugal compressor; Shrouded impeller; Stability; Instability; Rotating stall; Surge.

Student Number : 2015-22709

Contents

Abstract ..... **i**

Contents ..... **iii**

List of Figures ..... **v**

List of Tables ..... **viii**

Nomenclature ..... **ix**

Chapter 1. Introduction **1**

1.1. Background 1

1.2. Thesis Objectives 4

1.3. Outline of Thesis 5

Chapter 2. Experimental Setup **8**

2.1. Test Facility 8

2.2. Test Section Design 9

2.3. Instrumentation 10

2.4. Experimental Configuration 17

2.5. Test Procedure 18

Chapter 3. Baseline Compressor Characteristic **26**

3.1. Steady Performance – Pressure Rise 26

3.2. Unsteady Compressor Response 27

Chapter 4. Eccentricity Effects on Stability 45

4.1. Effects of Eccentricity on Steady Performance – Pressure Rise 45

4.2. Influence of Eccentricity on the Onset of Rotating Stall and Surge 46

4.3. Unsteady Compressor Response against Eccentricity 47

Chapter 5. Conclusions 55

Bibliography 56

Appendix A. Calibration 60

Abstract in Korean 65

List of Figures

Figure 1.1. Schematic of a shrouded centrifugal compressor 6

Figure 1.2. Surge and rotating stall 6

Figure 1.3. Schematic description of eccentricity 7

Figure 2.1. Schematic of a turbocharger System.....19

Figure 2.2. Test shrouded impeller.....19

Figure 2.3. The front view of a test section.....20

Figure 2.4. Overview of instrumentation 21

Figure 2.5. Locations of Kulite sensors.....21

Figure 2.6. Diagram of steady measurement system.....23

Figure 2.7. Diagram of unsteady measurement system and control system 24

Figure 2.8. Gap sensor installation.....25

Figure 3.1. Overall total-to-static pressure rise coefficient versus flow coefficient 35

Figure 3.2. Spectrogram of pressure data at diffuser inlet 36

Figure 3.3. Spectrogram at each meridional positio.....36

Figure 3.4. Magnitude of Spatial Fourier Transform coefficients at diffuser inlet 37

Figure 3.5. Phase of Spatial Fourier Transform coefficients at diffuser inlet.....38

Figure 3.6. Impeller inlet Kulites: path-time graph and corresponding spectrograms of 0th, 1st, 2nd, 3rd, and 4th spatial Fourier coefficients. 39

Figure 3.7. Diffuser inlet Kulites: path-time graph and corresponding spectrograms

of 0th, 1st, 2nd, 3rd, and 4th spatial Fourier coefficients. 40

Figure 3.8. Seal inlet Kulites: path-time graph and corresponding spectrograms of 0th, 1st, 2nd, 3rd, and 4th spatial Fourier coefficients.....41

Figure 3.9. Seal gland Kulites: path-time graph and corresponding spectrograms of 0th, 1st, 2nd, 3rd, and 4th spatial Fourier coefficients.....42

Figure 3.10. Pressure traces into surge at impeller inlet, at diffuser inlet, at seal inlet, and seal gland. 43

Figure 3.11. Traveling Wave Energy of the second harmonic at impeller inlet, at diffuser inlet, at seal inlet, and at seal gland.....43

Figure 3.12. PSD magnitude of zeroth harmonic at zero frequency 44

Figure 4.1. Overall total-to-static pressure rise coefficient vs. flow coefficient 49

Figure 4.2. Impeller total-to-static pressure rise coefficient vs. flow coefficient..... 49

Figure 4.3. Diffuser static-to-static pressure rise coefficient vs. flow coefficient 50

Figure 4.4. The onset of rotating stall and surge 50

Figure 4.5. Case 2: Diffuser inlet Kulites: path-time graph and corresponding spectrograms of 0th, 1st, 2nd, and 3rd spatial Fourier coefficients. (Surge, $\phi = 0.0440,\ e = 19.6\%$) 51

Figure 4.6. Case 3: Diffuser inlet Kulites: path-time graph and corresponding spectrograms of 0th, 1st, 2nd, and 3rd spatial Fourier coefficients. (Rotating stall, $\phi = 0.0448,\ e = 26.2\%$).....51

Figure 4.7. Case 4: Diffuser inlet Kulites: path-time graph and corresponding spectrograms of 0th, 1st, 2nd, and 3rd spatial Fourier coefficients. (Rotating stall, $\phi = 0.0452,\ e = 37.8\%$) 52

Figure 4.8. Case 4: Diffuser inlet Kulites: path-time graph and corresponding spectrograms of 0th, 1st, 2nd, and 3rd spatial Fourier coefficients. (Surge, $\phi = 0.0441,\ e = 37.8\%$) 52

Figure 4.9. Case 5: Diffuser inlet Kulites: path-time graph and corresponding spectrograms of 0th, 1st, 2nd, and 3rd spatial Fourier coefficients. (Rotating stall, $\phi = 0.0463,\ e = 58.7\%$) 53

Figure 4.10. The number of stall cells against eccentricity 54

Figure 4.11. The frequency of rotating stall cells against eccentricity 54

Figure A.1. Description of calibration jig 61

Figure A.2. Chamber inside the calibration jig 61

Figure A.3. Flush mounting and non-flush mounting 61

Figure A.4. The results of Kulite calibration (left-to-right order): (a) One example of Kulite calibration results, (b) Raw signal of Kulite sensor during purge, (c) FFT value of raw signal during purge, (d) Cross correlation of Kulite sensors located at same distance from inlet and outlet 63

Figure A.5. Calibration of gap sensors 64

Figure A.6. Results of gap sensor calibration and repeatability check 64

List of Tables

Table 2.1. Compressor design values 20

Table 2.2. Specification of gap sensor 22

Table 2.3. Specification of Kulite sensors 22

Table 2.4. Kulite sensor information against meridional positions 22

Table 2.5. Test configuration 25

Nomenclature

m	Mass flow rate
a	Speed of sound
M	Mach number
T	Temperature
T_0	Reference temperature
P	Pressure
P_0	Reference pressure
N	Rotational speed
D	Diameter
ϕ	Flow coefficient, $\frac{m}{\rho N D^3}$
ψ	Pressure rise coefficient, $\frac{P_{in} - P_{out}}{\rho N^2 D^2}$
θ	Circumferential angle
R	Radius
b	Diffuser width
s	Distance
ε	Offset distance
e	Eccentricity
δ	Nominal labyrinth seal clearance
a_k	k-th harmonic coefficient
B	B-parameter, eqn (3. 4) and (3. 5)
U	Mean impeller speed
A_c	Compressor through-flow area
L_c	Effective length of compressor duct

V_p	Volume of plenum
ω_H	Helmholtz frequency
V	Velocity

Subscript

1	Impeller inlet
2	Impeller outlet (or diffuser inlet)
3	Diffuser outlet
h	Hub
t	Tip
amb	Ambient condition

Chapter 1. Introduction

1.1. Background

Compressors are used in aircraft engines, power plants, transportation, process machine, and other wide applications. Compressors are usually categorized into axial compressor and centrifugal compressor by flow direction. Centrifugal compressors also have two types, which are shrouded centrifugal compressor and unshrouded centrifugal compressor, by impeller shapes. Impeller in a shrouded centrifugal compressor has a shroud on blades while impeller in an unshrouded centrifugal compressor has exposed blades. Due to a shroud on blades, shrouded centrifugal compressor has a leakage from impeller downstream to upstream along the secondary flow passage between a shroud and a casing. Therefore, designers put labyrinth seals on the eye of an impeller to reduce leakage through the secondary passage (Figure 1.1).

Instability

Aerodynamic instability has been occurred in all kinds of compressors and limits operating range to avoid damages of machines. Aerodynamic instability includes surge and rotating stall. Surge is one-dimensional oscillation which have annulus averaged mass flow through total compression system, while rotating stall is two-dimensional, sometimes three-dimensional, rotating flow along circumferential direction in a compressor (Figure 1.2). There has been much efforts

to understand surge and rotating stall. First detailed research was the work by Emmons et al. [7]. Emmons et al. [7] measured unsteady flow instability by hot wires and established an instability model in an isolated cascade.

In axial compressors, early studies focused on the onset of surge and rotating stall. Greitzer [12] published the theoretical surge model of a compression system with eigenvalue problems to predict the onset of surge and to describe mechanisms of surge in 1976. Moore and Greitzer [19] and Greizter and Moore [12] established the rotating stall model with actuator disc theory. Hynes et al. [15] studied the effects of circumferential inlet flow distortion on the onset of flow instability. In 1990s and 2000s, much research focused on the inception, warning schemes, and active controls of surge and rotating stall ([4], [14], [17], and [24]). In recent days, the origins of rotating stall has been studied in the view of detailed flow field inside the blade passage ([16], [20], and [25]). Therefore, considerable studies have explored instability in axial compressors. The history of research on surge and stall in axial compressors is described in the paper of Day [5] in detail. In contrast of axial compressors, instability research in centrifugal compressors has not been conducted in much detail relative to axial compressors because centrifugal compressor has very complex flow field, which arises from radial flow in an impeller and a diffuser. For this reason, Abdelhamid [1] and Frigne [9] studied a stall model for vaneless diffuser in 1980 and 1984, respectively. Later, Spakovszky [22] established a total centrifugal compression system model in 2001. In recent days, instability in a return channel has been considerably studied. However, research in centrifugal compressors has been still in fundamental research regarding the onset and the inception of surge and rotating stall.

Eccentricity

Eccentricity arises due to discrepancy of center positions between a rotor and a counterpart (Figure 1.3). There are many sources of eccentricity—misalignment, rotor bending, tilted shaft in overhung type rotor, less stiff bearing (especially journal bearing), and rubbing due to unwanted stall events. Eccentricity causes first harmonic non-axisymmetric flow in a compressor; then, non-axisymmetric flow may affect the onset of rotating stall. Graf et al. [11] published the first study of non-axisymmetric tip clearance effects on stability of an axial compressor in 1997. They extended a Moore-Greitzer model with non-axisymmetric tip clearances and validated their model with experimental data. They reported that eccentricity exerts bad influence on the performance and the onset of rotating stall as a result of flow redistribution along circumferential direction. Cameron et al. [4] studied the effects of flow non-uniformity in an axial compressor due to steady eccentricity and rotor whirling on stall inception. Young et al. [26] conducted experiments and CFD analysis with Immersed Boundary Method with Smeared Geometry (IMBSG) to predict compressor performance accounting of eccentricity. In contrast of research in axial compressors, eccentricity effects on stability have not been investigated in centrifugal compressors even though eccentricity has been more commonly occurred in centrifugal compressors.

Eccentricity in axial compressors provides non-axisymmetric tip clearance; then, tip flow across blades is influenced. In contrast, eccentricity in shrouded centrifugal compressors, leads to non-axisymmetric seal clearance, which is an important parameter when designing shrouded centrifugal compressors. Therefore,

circumferential flow redistribution in the secondary passage arises mainly across labyrinth seals and this redistributed secondary flow comes in the main flow to the impeller. Due to the different influence of eccentricity on flow redistribution between axial and centrifugal compressors, the effects of eccentricity on stability in shrouded centrifugal compressors have not been directly anticipated with the research of axial compressors.

1.2. Thesis Objectives

The thesis experimentally examines the effects of eccentricity on stability of a high-speed shrouded centrifugal compressor. The specific objectives to be addressed are as follows.

(1) To identify the characteristics of instability of a high-speed shrouded centrifugal compressor when in concentric condition.

(2) To evaluate how eccentricity influences the performance, which is pressure rise coefficient, of a compressor.

(3) To evaluate how eccentricity affects the onset and the behavior of rotating stall and surge.

1.3. Outline of Thesis

The thesis is organized in the following manner.

Chapter 2 describes the details of test facility, test section design, instrumentation, test configuration, and test procedure. Instrumentation to measure unsteady phenomena is explained in detail. Chapter 3 presents the compressor unsteady behavior in concentric condition including the onset of instability, the number and the speed of rotating stall cells. Chapter 4 examines the effects of eccentricity on stability. Chapter 5 provides the conclusions. Appendix A gives the method and the results of sensor calibration.

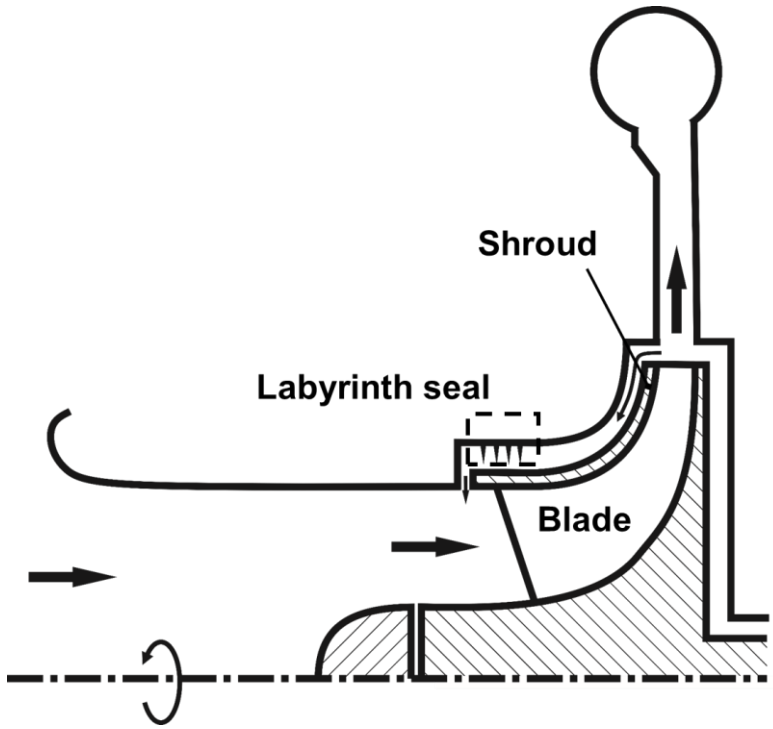

Figure 1.1. Schematic of a shrouded centrifugal compressor

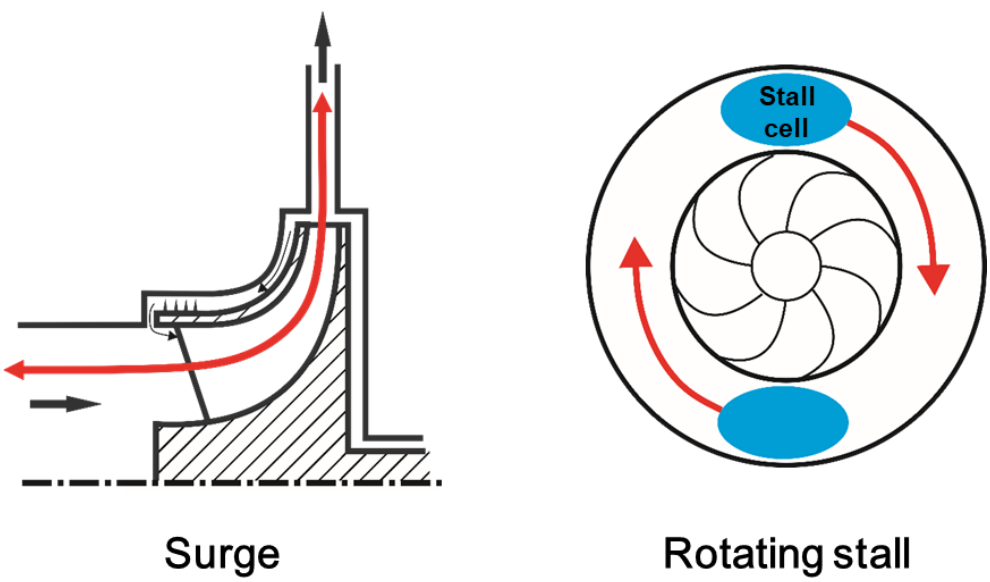

Figure 1.2. Surge and rotating stall

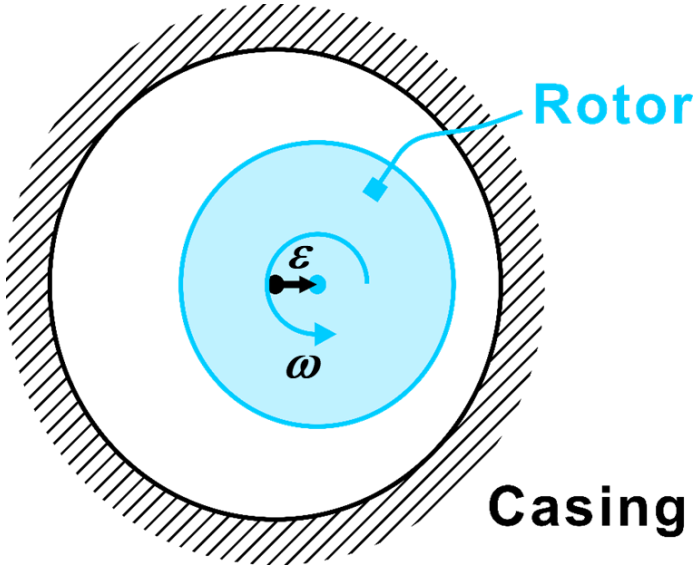

Figure 1.3. Schematic description of eccentricity

Chapter 2. Experimental Setup

As discussed in the previous chapter, effects of non-axisymmetric clearance exacerbate instability in axial compressors but have not been investigated in centrifugal compressors. To measure instabilities regarding eccentricity, a test section is re-designed to apply eccentricity as the first harmonic non-axisymmetric clearance by moving casings rather than the shaft of a turbocharger with highly accurate shims. Instrumentation has been setup to obtain the compressor performance and the unsteady compressor behavior.

2.1. Test Facility

Experiments have been conducted with a turbocharger test rig in Korea Aerospace Research Institute (KARI). Test facility consists of a blower, a turbocharger, and a lubrication system as shown in a schematic drawing (Figure 2.1). Turbocharger system is divided into a turbine section and a compressor section. In Figure 2.1, a blower provides high pressure air to a turbine of a turbocharger. Then, a turbine generates power to rotate a rotor of a turbine charger and a compressor works. Flow rate through a turbine can be controlled with a 3-way valve and an inlet valve, and flow rate through a compressor can be controlled with two throttle valves at the exit of a compressor. For safety when going to surge, a surge valve is installed at the exit of compressor. In the research, test section is a

compressor part of a turbocharger (Figure 2.3). Then, rotational speed of a compressor is mainly adjusted by 3-way valve and inlet valve and mass flow rate through a compressor is determined by the level of throttle valves at the exit of a compressor.

2.2. Test Section Design

Re-designed and manufactured parts are an impeller, a diffuser, and casings. The detailed design and manufacturing have been supported by Hanhwa Techwin. Table 2.1 shows the design values of the compressor.

Impeller

An impeller has been designed to meet the requirement of design flow rate, design pressure ratio, condition at compressor inlet and outlet, and geometrical constraints. The test impeller is a shroud type and the number of blades is sixteen. The exit diameter is 153 mm and backsweep angle is 44.5 degree. Material of the impeller is Titanium. The picture of the test impeller is Figure 2.2.

Diffuser

The vaneless diffuser has been applied in the compressor. The diffuser has a width of 9.19 mm and is the unpinched type. The radius ratio of diffuser inlet and diffuser outlet is 1.7 and downstream flow enters a collector.

Casings

The main consideration to design casings is how to move casings or rotor. In the related research of the thesis, Graf et al. [11] used stepped casings to make non-axisymmetric tip clearance and Young et al. [26] moved casings in one way with measuring relative position of centerline between a rotor and casings by using a dial gauge. The research of this thesis has also applied casing offset for eccentricity by using highly accurate shims.

The shape of a shroud on the casings has the same topology of the shroud on the impeller. Labyrinth seal at the eye of the impeller has been placed on the casing (so called, seal on stator). The number of labyrinth seal teeth is four. The width and height of labyrinth seal has been designed with the same dimension.

2.3. Instrumentation

In the research, steady parameters and unsteady behavior have been measured as illustrated in Figure 2.4 and Figure 2.5. The steady compressor parameters include rotational speed, pressure rise coefficient, flow coefficient, and eccentricity. The unsteady pressure response has been obtained by fast response pressure sensors (Kulite sensors).

Ambient condition

Ambient condition includes pressure, temperature, and relative humidity. Ambient pressure has been measured with MKS 690A. The MKS 690A pressure transducer has a range of 0 – 1000 mmHg and an accuracy of 0.12% reading. Ambient temperature has been measured by a k-type thermocouple which has an accuracy of ±0.4 K. Relative humidity has been measured by Humlog20 (range of 10 – 95 %RH and accuracy of ±2% RH). Humlog20 also measures ambient pressure (accuracy of ±50 Pa) and temperature (accuracy of ±0.3 K) but they are only used for reference. MKS 690A, thermocouple, and Humlog20 are installed at the same location near the compressor.

Static pressure

Static pressures have been measured at five meridional locations, which are bellmouth throat, impeller inlet, diffuser inlet, diffuser outlet, and collector. All static pressures have been measured by Netscanner 9116, Netscanner 9016, and Netscanner 9816 transducers (ranges of 5 psid, 15 psid, and 30 psid dependent on the meridional positions, and accuracy of ±0.05% F.S.). Eight static pressure taps at impeller inlet are located on the shroud casings at 5% impeller shroud radius away from the end of secondary flow passage. Eight static pressure taps at diffuser inlet and diffuser outlet are installed on the shroud casings at 105% and at 170% impeller radius, respectively. At collector, pressures have been also measured to monitor steady state condition. For reference, pressures at upstream and downstream of a turbine in a turbocharger have been measured.

Total pressure and total temperature

Four Kiel total temperature and pressure probes have been installed at diffuser outlet, 170% impeller radius with circumferentially equal positions. Kiel probes have k-type thermocouples and nozzled total pressure tubes. Pressures have been measured by Netscanner 9116 transducers (range of 30 psid and accuracy of ±0.05% F.S.). Kiel total temperature and pressure probes were aligned at the same direction with flow direction at design flow coefficient.

At diffuser outlet (170% impeller radius), Four k-type thermocouple have been installed with circumferentially equal positions. To measure total temperature effectively, thermocouple had been designed with bared type at upstream direction but coved by half cylindrical stainless tube at the opposite side. All thermocouples applied in the research have an accuracy of ±0.4 K.

Rotational speed

Rotational speed has been measured by a remote optical tachometer (ROS-HT-W-25, Monarch Instrument). Reflective tape is attached at one side of the nose cone in front of the test impeller with 40° circumferential angle. Optical tachometer has a range of 0 – 50,000 rpm and works under temperature of -25° to 125°C. Output signal has a format of TTL. Then, DAQ system can recognize TTL signal as digital signal. In the measurement program in a DAQ system, rise in TTL signal is used to count rotational speed and four counts are averaged.

Flow coefficient

Bellmouth has been used to measure mass flow rate at the inlet of a

compressor. Four static pressures have been measured with Netscanner 9116 pressure transducers (range of 5 psid and accuracy of ±0.05% F.S.) at the throat of a bellmouth. Measured pressure has been converted to corrected mass flow rate with the equation (2. 1) and bellmouth has been calibrated in Korea Research Institute of Standards and Science (KRISS).

$$m_{corrected} = m\frac{\sqrt{T_{amb} / T_0}}{P_{amb} / P_0} = ftn(\Delta P) \quad (2.\ 1)$$

(ftn : calibration function)

From the measurement of pressure, temperature, rotational speed and mass flow rate, flow coefficient has been computed with the equation (2. 2).

$$\phi = \frac{m}{\rho N D_2^3} \quad (2.\ 2)$$

Pressure rise coefficient

To evaluate steady-state performance of a compressor, total-to-static pressure rise coefficient has been used in the research. Total-to-static pressure rise coefficient is defined as below (2. 3).

$$\psi_{ts} = \frac{P_{3s} - P_{1t}}{\rho N^2 D_2^2} \quad (2.\ 3)$$

Eccentricity

Eccentricity is defined as centerline offset divided by nominal labyrinth seal clearance, the equation (2. 4). Therefore, eccentricity is zero when centerline offset is zero, while eccentricity is 1 when the shroud of an impeller meets casings.

$$e = \varepsilon / \delta \tag{2. 4}$$

Centerline offset has been measured by perpendicularly installed gap sensors (AEC PF-03 probes and CFC-03 converter, Table 2.2). The PF-03 sensors has a range of 0 – 1 mm and a linearity of 1% F.S. Gap sensor can measure high speed data because CFC-03 converter has a high frequency characteristic. Therefore, to monitor the motion of the rotor (static eccentricity or whirling), the data has been collected at the rate of 204.8 kHz. Nonetheless, for the reason that the range of distance in this research is 0 – 1.5 mm and the shroud was made by different material with factory calibration, PF-03 sensors had been re-calibrated. From measurement, following reduction equations (2. 5), (2. 6) are used to calculate centerline offset.

$$\varepsilon_x = R_{sensor} - R_{shroud} - s_{measure,x} \tag{2. 5}$$
$$\varepsilon_y = R_{sensor} - R_{shroud} - s_{measure,y} \tag{2. 6}$$

In above equations, R_{shroud} is a design parameter and $s_{measure}$ is measurement, but R_{sensor} is unknown because R_{sensor} is dependent on installation. Then, R_{sensor} was measured by a coordinate measurement machine (CMM) after

installation of gap sensors to casings. From these calculation, the magnitude and the phase of eccentricity can be achieved.

Unsteady pressure

To measure rotating stall and surge, fast response pressure transducres (Kulite sensors) have been installed at impeller inlet, diffuser inlet, labyrinth seal inlet and the 2nd labyrinth seal gland. At each meridional position, eight Kulite sensors locate circumferentially equal spacing. Then, the total number of Kulite sensors is thirty two in the research. At the impeller inlet, the model of Kulite sensors is XCQ-062 and the pressure range is 5 psid. At other meridional positions, the model of Kulite sensors is XCE-062 and the pressure range is 30 psid. All sensors acquire data at the rate of 204.8 kHz to obtain at least 15 samples in one blade passing for further research. The specification of Kulite sensors used in this research is summarized in Table 2.3 and sensor information at each meridional position is shown in Table 2.4. All sensors have been calibrated and calibration is described in Appendix A.

Accelerometer

Four two-axis accelerometer have been used to monitor vibration for safety. Locations of accelerometers are a bearing housing of a turbocharger, a shroud casing of a compressor in the turbocharger, a casing of a turbine in the turbocharger and a collector. At each location, vibration has been monitored for shaft and rotating direction.

Data Acquisition System (DAQ system)

DAQ systems are divided into two parts, steady DAQ and unsteady DAQ. Figure 2.6 and Figure 2.7 illustrates steady and unsteady DAQ systems, respectively. Steady DAQ system acquires data at the relatively low sampling rate and unsteady DAQ system acquires data at the very high sampling rate. Therefore, steady DAQ system obtains data from steady sensors, such as Netscanner pressure transducers, MKS pressure transducers, gap sensors, optical tachometer, thermocouple, and valves. On the other hand, unsteady DAQ system acquires only Kulite sensors, gap sensors, and a MKS pressure transducer at bellmouth throat.

For steady measurement, PSI communicates directly with DAQ computer by TCP/IP communication. Voltage from gap sensors and MKS sensors for ambient pressure has been converted to digital signal by PXI-4472B A/D converter. TTL from an optical tachometer has been connected to digital input port of PXI-6251. Thermocouple signal has been amplified and collected by SCXI-1102. Current feedback from two throttle valves, 3-way valve, and inlet valve has been measured by SCXI-1313 and SCXI-1125 which have highly precise resistance.

For unsteady measurement, voltage signal from 32 Kulite sensors has been simultaneously measured by PXI-4495. PXI-4495 has 24-bit resolution and acquire data up to 204.8 kHz sampling rate. Voltage from gap sensors and an MKS sensor for pressure at the bellmouth throat has been collected by PXI-4492 which has same specification regarding resolution and sampling rate. All the data to PXI-4495 and PXI-4492 have been saved in a high-capable and high-speed data storage system.

Control system

Control system has been separated from data acquisition system (DAQ system) to make an immediate command to valves when instability occurs. Control system includes valve controls of two throttle valves, an inlet valve, a 3-way valve, and a surge valve. Control computer controls two throttle valves by 4 to 20 mA current. An inlet valve, a 3-way valve, and a surge valve have been controlled by stand-alone control box. An inlet valve and a 3-way valve have current input as 4 to 20 mA and a surge valve has voltage input of 220 V.

Uncertainty of main parameters

The uncertainty of pressure rise coefficient (ψ) is 0.647%. The uncertainty of flow coefficient (ϕ) is 1.04%. The uncertainty of eccentricity (e) is 1.10%. Uncertainty values are calculated by using Root-Sum-Square Method.

2.4. Experimental Configuration

The centerline of shroud casings has been altered to assess sensitivity of performance and instability with the level of eccentricity. To alter the centerline of shroud casings, highly accurate thickness shim has been shimmed out and in to the desired eccentricity. The test matrix of experiments is summarized in Table 2.5. Test eccentricities are 9.6%, 19.6%, 26.2%, 37.8%, and 58.7%. The test case of 9.6% eccentricity is the baseline as a concentric case in the research.

2.5. Test Procedure

Steady test and unsteady test have been separately performed. Steady test is to obtain a compressor performance map and unsteady test is to measure instabilities. All tests are conducted at a 100% design speed, 40,000 rpm. At each eccentricity case, steady test precedes unsteady test. In steady tests, pressure rise coefficient, flow coefficient, eccentricity and other parameters are measured by reducing flow coefficient until expected flow coefficient of rotating stall and surge. To check repeatability, steady tests have been repeated. After steady tests, throttle valves are set to slightly bigger flow coefficient of expected instability and are gradually closed. During closing throttle valves, DAQ system collects and stores all data of Kulite sensors, mass flow rate, and gap sensors. This measurement keeps continuing until surge occurs. At every end of tests, casings are disassembled and re-assembled to adjust eccentricity.

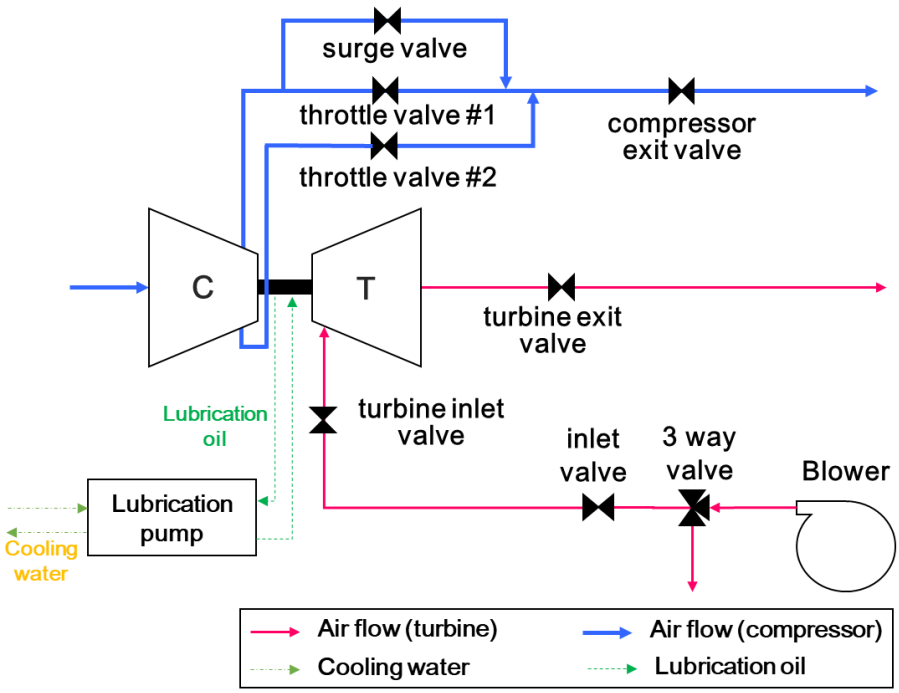

Figure 2.1. Schematic of a turbocharger System

Figure 2.2. Test shrouded impeller used in the reserach

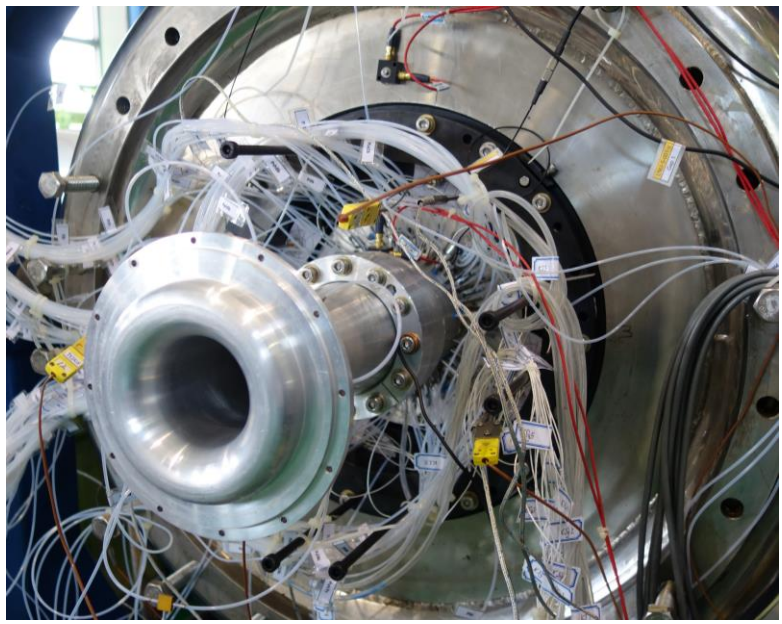

Figure 2.3. The front view of a test section

Item		Value
Compressor	Rotational Speed (N)	40,000 rpm
	Flow Coefficient (ϕ)	0.0632
	Pressure Rise Coefficient (ψ_{t-s})	0.55
	Impeller exit tip Mach number (M_{tip})	0.85
Impeller	Type	Shrouded
	Number of blades	16
	Inlet Hub Diameter ($2R_{1h}$)	30.2 mm
	Inlet Shroud Diameter ($2R_{1t}$)	87.6 mm
	Exit Diameter ($2R_2$)	153 mm
	Backsweep Angle (from radial)	44.5 deg
	Nominal Seal Clearance (δ)	0.91 mm
Diffuser	Type	Vaneless
	Diffuser Width (b_2)	9.19 mm
	Radius ratio (R_3 / R_2)	1.7

Table 2.1. Compressor design values

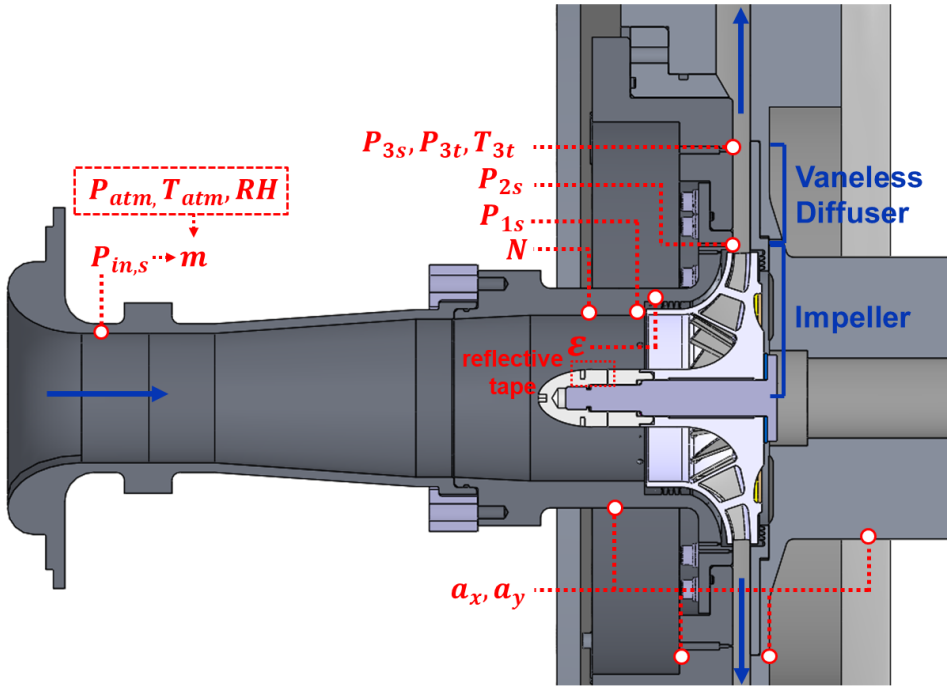

Figure 2.4. Overview of instrumentation

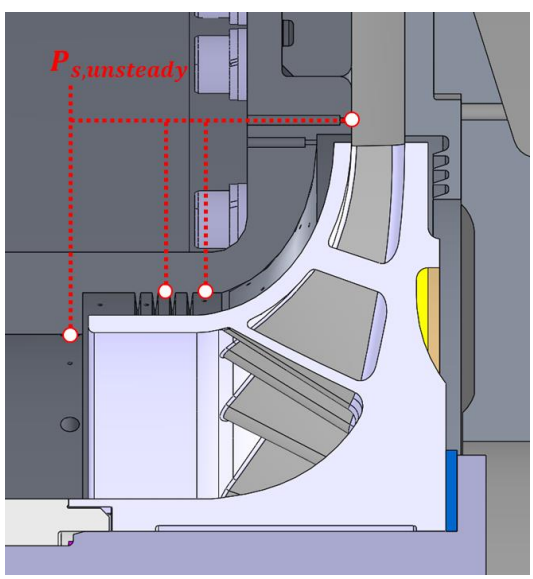

Figure 2.5. Locations of Kulite sensors

Model	PF-03	CFC-03
Measuring range (iron)	0 to 1 mm	
Dead zone	0 mm	
Output voltage	0 to 5 V	
Resolution	1.2 μm	
Linearity	1% F.S.	
Temperature range	-20°C to +140°C	
Frequency characteristics		DC to 20 kHz -2dB

Table 2.2. Specification of gap sensor

Model	XCQ-062	XCE-062
Pressure Range	5 psid	30 psid
Non-linearity	0.1% F.S.	
Hysterisys	0.1% F.S.	
Repeatibility	0.1% F.S.	
Resolution	Infinitesimal	
Natural Frequency	150 kHz	240 kHz
Diameter	1.7 mm	
Length	9.5 mm	

Table 2.3. Specification of Kulite sensors

	Impeller Inlet	Diffuser Inlet	Seal Inlet	Seal Gland
Range	5 psid	30 psid	30 psid	30 psid
Number	8	8	8	8
Flush mounting	Yes	Yes	No	No
Amplifier	Ext. amp	Int. amp	No	No
Position	$0.05R_{shroud}$	$1.05R_{imp}$		

Table 2.4. Kulite sensor information against meridional positions

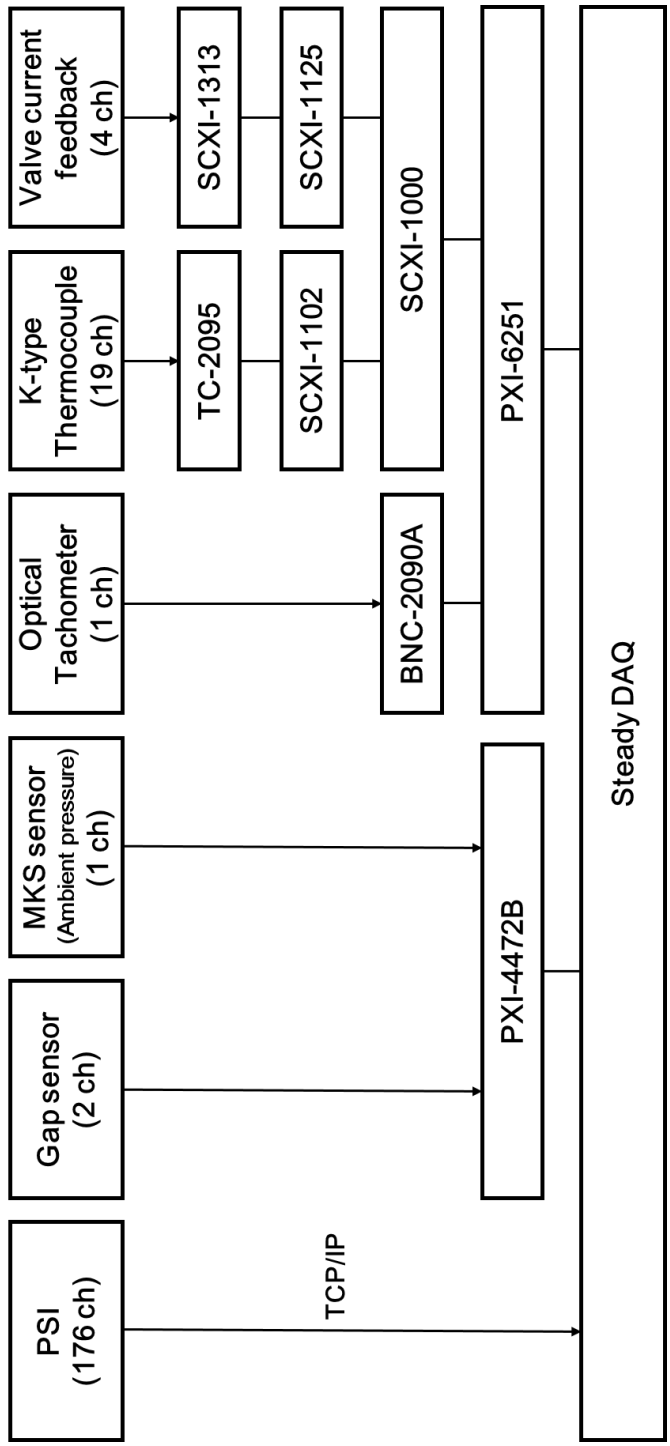

Figure 2.6. Diagram of steady measurement systems

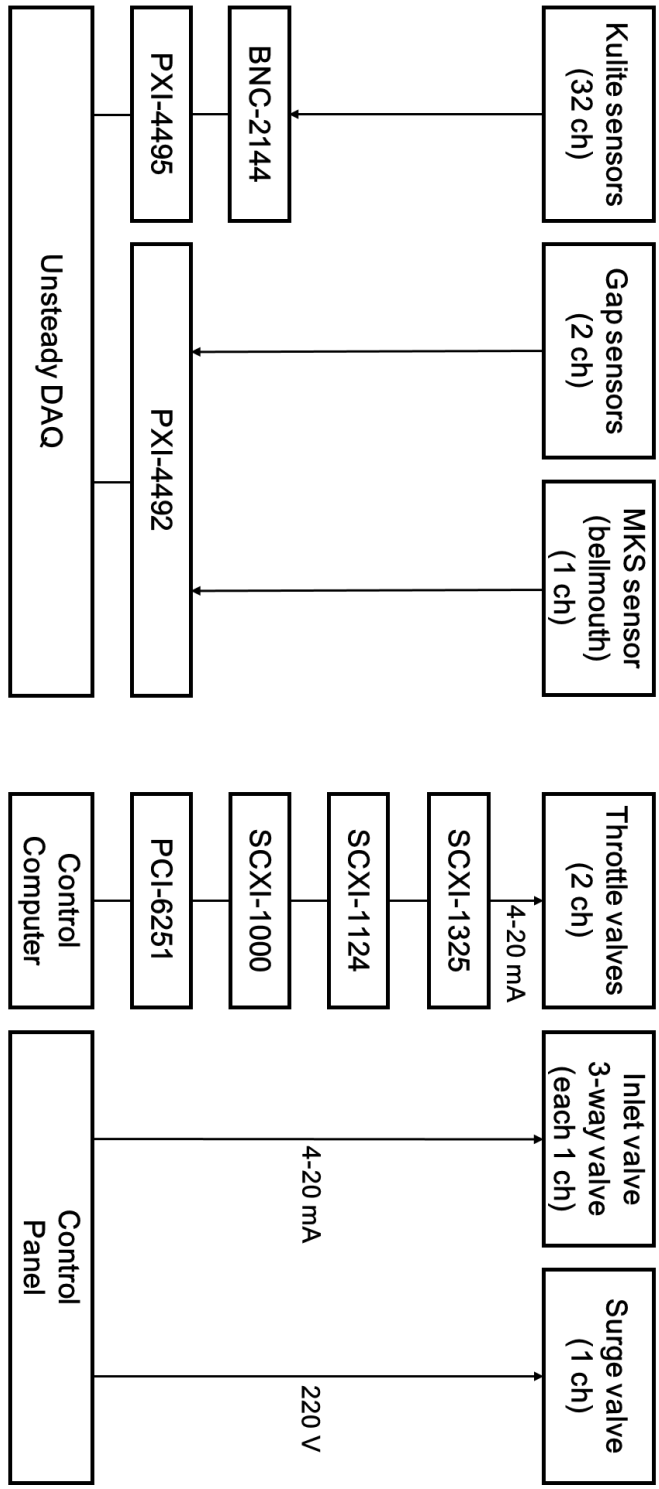

Figure 2.7. Diagram of unsteady measurement system and control system

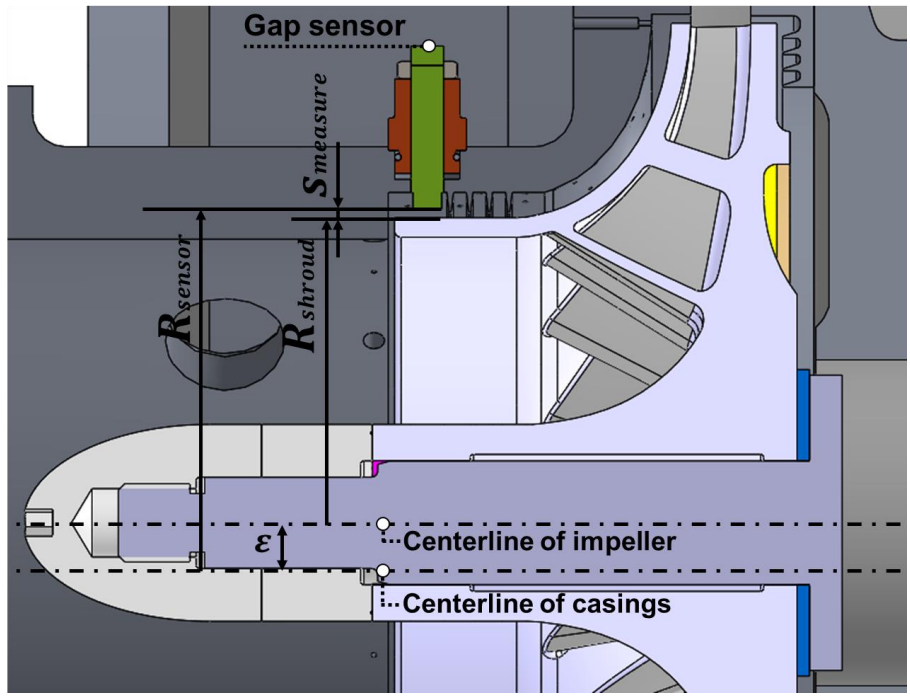

Figure 2.8. Gap sensor installation

Item	Centerline Offset (ε)	Eccentricity (e)
Case 1 (Baseline)	0.087 mm	9.56 %
Case 2	0.178 mm	19.6 %
Case 3	0.238 mm	26.2 %
Case 4	0.344 mm	37.8 %
Case 5	0.534 mm	58.7 %

Table 2.5. Test configuration

Chapter 3. Baseline Compressor Characteristics

Chapter 3 describes compressor characteristics of a test compressor in concentric condition. Steady and unsteady measurement have been done for case 1 as a baseline in Table 2.5. The objectives of the chapter 3 are as follows.

(1) To obtain the pressure rise coefficient against flow coefficient at concentric condition.

(2) To understand instabilities including

A. the type of instability of the compressor;

B. the number of rotating stall cells;

C. the speed of rotating stall;

D. the location where instability arises; and

E. the surge behavior.

3.1. Steady Performance – Pressure Rise Coefficient

Figure 3.1 shows the graph of total-to-static pressure rise coefficient at 100% design speed line. Circle indicates steady measurement at each flow coefficient and diamond indicates instantaneous measurement when surge occurs. The compressor has flow coefficient of 0.08 at choking and 0.063 of design flow coefficient. The compressor goes into rotating stall and surge at flow coefficient of 0.044.

3.2. Unsteady Compressor Response

Section 3.2. includes the results of unsteady pressure data from fast response pressure transducers (Kulite sensors). Three kinds of instabilities have been established as rotating stall, surge, and classic surge. As described in Chapter 1, rotating stall is two-dimensional flow rotation of stall cells in circumferential direction and surge is one-dimensional flow oscillation along total compression system. Classic surge as the third instability is the combined instability of surge and rotating; therefore, when classic surge occurs, rotating stall goes in and out during surge process simultaneously. Classic surge has been sometimes reported in high speed centrifugal compressors which have same order between inertial forces and pressure differential forces in B-parameter (Schleer [21], Spakovszky [22]). To figure out which instability the compressor suffers from and how rotating stall cells behave, the method of Short Time Fourier Transform (STFT), Spatial Fourier Transform (SFT), and Traveling Wave Energy (TWE) are applied to data of Kulite sensors.

3.2.1. Short Time Fourier Transform (STFT or Spectrogram)

Fourier transform is a good method to decompose from time domain signal to frequency domain but the result of Fourier transform does not include time data. The research has focus on transient response of pressure data. Therefore, applying only Fourier transform to pressure data is not sufficient only to capture the exact onset of rotating stall and surge but also to

understand transient responses. To add time information to Fourier transform, Fourier Transform (or FFT) with small windows of data has been conducted iteratively along time. This method is called short time Fourier transform (STFT) or spectrogram.

Figure 3.2 depicts the result of Short Time Fourier Transform at diffuser inlet when surge occurs (the diamond point in Figure 3.1). Time axis is non-dimensional time in revolution and time at zero indicates the onset of surge. Frequency is non-dimensionalized by rotational speed of the impeller. Three peaks have been shown in the Figure 3.2. Frequency of 16 exists at all time, but frequencies of zero and 0.19 comes out at certain time, then, disappears. To see more specifically, peak at 16 of frequency indicates blade passing frequency (BPF) because the number of impeller blades is sixteen. Two peaks at relatively small frequencies have larger amplitude than the amplitude at blade passing frequency. Figure 3.3 illustrates spectrograms which show details in the frequency range from 0 to 1.5 at impeller inlet, diffuser inlet, seal inlet, and seal gland. At all meridional locations, a peak at zero frequency appears. On the other hand, a peak at 0.19 frequency appears at only diffuser inlet. Two other peaks are assumed to be rotating stall and surge. However, this spectrogram is not sufficient to describe whether instabilities occur or not.

3.2.2. Spatial Fourier Transform (SFT)

To clarify whether those peaks in Short Time Fourier Transform indicate rotating stall or surge, Spatial Fourier Transform needs to be applied to circumferentially located eight Kulite sensors at each meridional position.

Spatial Fourier Transform divides spatially distributed signals into spatially periodic functions, while FFT divides pressure signal into timely periodic functions. The equation (3. 1) is a definition of Spatial Fourier Transform.

$$\delta P(\theta,t) = \mathrm{Re}\left[\int_{k=0}^{\infty} a_k(t)\cdot e^{ik\theta} dk\right] \tag{3. 1}$$

where δP is the pressure perturbation, θ is the circumferential location at one meridional position, and a_k is the spatial Fourier coefficient. If acquiring finite numbers of data along circumferential direction, discrete Spatial Fourier Transform is applied to data as shown in the equation (3. 2).

$$\delta P(\theta,t) = \mathrm{Re}\left[\sum_{k=0}^{N_{nyq}} a_k(t)\cdot e^{ik\theta}\right] \tag{3. 2}$$

where N_{nyq} is the Nyquist number to avoid aliasing in processing data. Nyquist number is determined by the number of sensors. From the equation (3. 2), spatial Fourier coefficient can be achieved by the equation (3. 3).

$$a_k(t) = \frac{1}{N}\sum_{n=1}^{N}\left\{\delta P(\theta_n,t)\cdot e^{ik\theta_n}\right\} \tag{3. 3}$$

Figure 3.4 and Figure 3.5 are the magnitude graph and the phase graph of first five spatial Fourier coefficients at diffuser inlet, respectively. Horizontal

axis is time in rotor revolution and zero indicates the onset of surge. Vertical axis is the magnitude of spatial Fourier coefficient and in Figure 3.4 and phase in radian in Figure 3.5. At -80 rotor revolution, magnitude of the second spatial harmonic coefficient starts to increase and the phase of the second harmonic coefficient increases linearly. However, other harmonics have relatively small magnitudes, and phases increase and decrease randomly. From Spatial Fourier Transform (SFT), the number of rotating stall cells can be found to be two and two cells have the speed of 0.19 rotor frequency. At 0 rotor revolution, the magnitude of zeroth order spatial harmonic coefficient suddenly increases but the indication of rotating stall disappears. These results at 0 rotor revolution have been understood that surge occurs.

3.2.3. Traveling Wave Energy (TWE)

From the method of Spatial Fourier Transform, the number and the speed of rotating stall cells can be found effectively in less noisy condition. Nonetheless, Spatial Fourier Transform is not effective in noisy condition. Tryfonidis [24] develops the Traveling Wave Energy (TWE) method to figure out the inception of rotating stall in noisy condition. The coefficients of Spatial Fourier Transform have both real and complex values. Therefore, when plotting power spectral density (PSD) of each coefficient of Spatial Fourier Transform, peaks at negative and positive frequencies can be acquired. This PSD divides signals into traveling and stationary waves with the negative PSD and the positive PSD. The details are explained in the works of Tryfonidis [24]. In general, rotating stall cells rotates at the same direction of

impeller in absolute frame, which is called forward traveling wave; then, a peak at rotating stall frequency show on only positive frequency spectra.

The pressure traces and the power spectra of 0th to 4th spatial Fourier coefficients at each meridional position are plotted in Figure 3.6 through Figure 3.9. At the graph of pressure traces, pressure signals of zero radian at the impeller inlet and seal gland have not been measured due to faulty during experiments. At the impeller inlet, rotating stall has not been measured but surge has been measured with zeroth order harmonic. At the diffuser inlet, rotating stall has been measured at the second harmonic and surge has been also measured at zeroth order harmonic. However, before the onset of rotating stall, pre-stall modes have been measured at the second and the third harmonics and one stall of third mode cell has the same speed of second mode. Small disturbances of rotating stall propagate to seal inlet but disappear at seal gland. In contrast of rotating stall, surge can be measured at all meridional positions at the zeroth harmonic.

3.2.4. Inception of Instability

Rotating stall

Two types of rotating stall inception have been reported for several years. One is modal type stall and the other is spike type stall. Modal type is two dimensional long wavelength pre-stall behavior and spike type is three dimensional short wavelength pre-stall behavior. From Figure 3.6 through Figure 3.9, modal waves have continuously measured at the second harmonic and the third harmonic. This modal waves are directly shown in the Figure

3.10. Before surge, strong modal waves develop gradually and become rotating stall. However, this modal wave is very weak at impeller inlet and at seal gland.

In the research, rotating stall has to satisfy one criteria: the amplitude of peak at rotating stall frequency is greater than the amplitude of the BPF peak. As confirmed in section 3.2.1., two peaks at zero and 0.19 frequencies have larger amplitude than the amplitude of the BPF peak. Then, to determine the exact onset of rotating stall, traveling wave energy has been computed and plotted in Figure 3.11. The onset of rotating stall is defined as time at half TWE of fully developed rotating stall. Kulite sensors at diffuser inlet have been detected rotating stall first, then, sensors at seal inlet, seal gland, impeller inlet have been detected in order. This propagation direction from diffuser to impeller describes rotating stall arises at the vaneless diffuser.

Surge

In the research, the onset of surge has been defined when the compression system transitions to fully developed surge. Therefore, the onset of surge has been defined as the time which has the maximum peak in power spectra of zeroth harmonic at impeller inlet. Figure 3.12 is PSD at zero frequency in zeroth harmonic. Surge can be detected at -10 revolution at diffuser inlet. Then, surge process starts and propagates to impeller inlet.

B-parameter

Greitzer defines two parameters, the B-parameter and the G-parameter, to

determine a surge stability. The B-parameter determines whether the compressions system suffer from rotating stall or surge. Greitzer defines the B-parameter as the equation (3. 4) and Spakovszky re-writes the B-parameter as the equation (3. 5).

$$B = \frac{U}{2a}\sqrt{\frac{V_p}{A_c L_c}} \tag{3. 4}$$

$$B = \frac{\frac{1}{2}\rho U^2 A_c}{\rho \omega_H U L_c A_c} \tag{3. 5}$$

Therefore, the B-parameter is interpreted as the magnitude of the pressure difference across the compressor duct divided by the driving for the acceleration of the fluid in the duct (Spakovszky [22]). Therefore, if the B-parameter is large, compression system will go into deep surge but if the B-parameter is small, compression system will go into rotating stall.

The B-parameter of the compressor in this research is 1.83. Then, the order of pressure and inertia forces are same. This B-parameter matches with the experimental data. In the results of Figure 3.6 through Figure 3.9, the compressor have modal type pre-curser and rotating stall precedes surge at -80 revolution. Also, rotating stall passes in and out during surge process. Therefore, the type of instability of this centrifugal compressor can be referred as the classic surge. Schleer [21] reported that a compressor goes into rotating stall when the compressor operates at lower speed and the compressor goes

into classic surge and surge as the compressor operates at an increased speed line. For this reason, classic surge has been reported in high-speed centrifugal compressors.

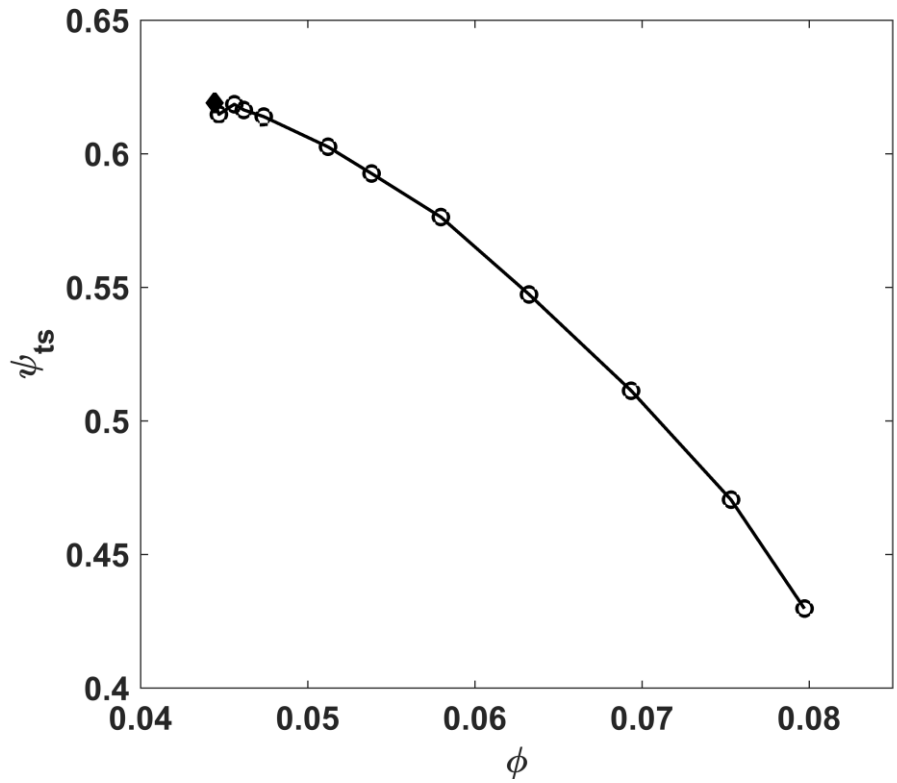

Figure 3.1. Overall total-to-static pressure rise coefficient versus flow coefficient

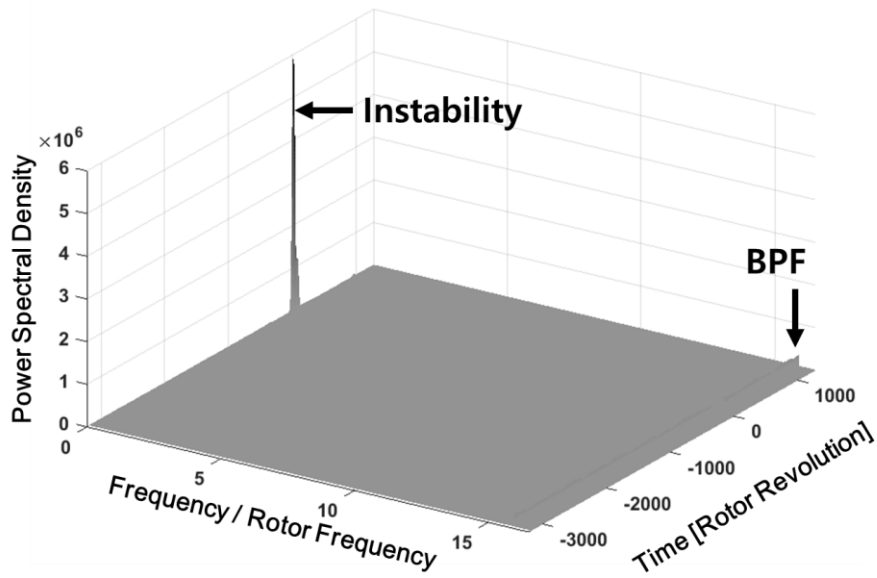

Figure 3.2. Spectrogram of pressure data at diffuser inlet

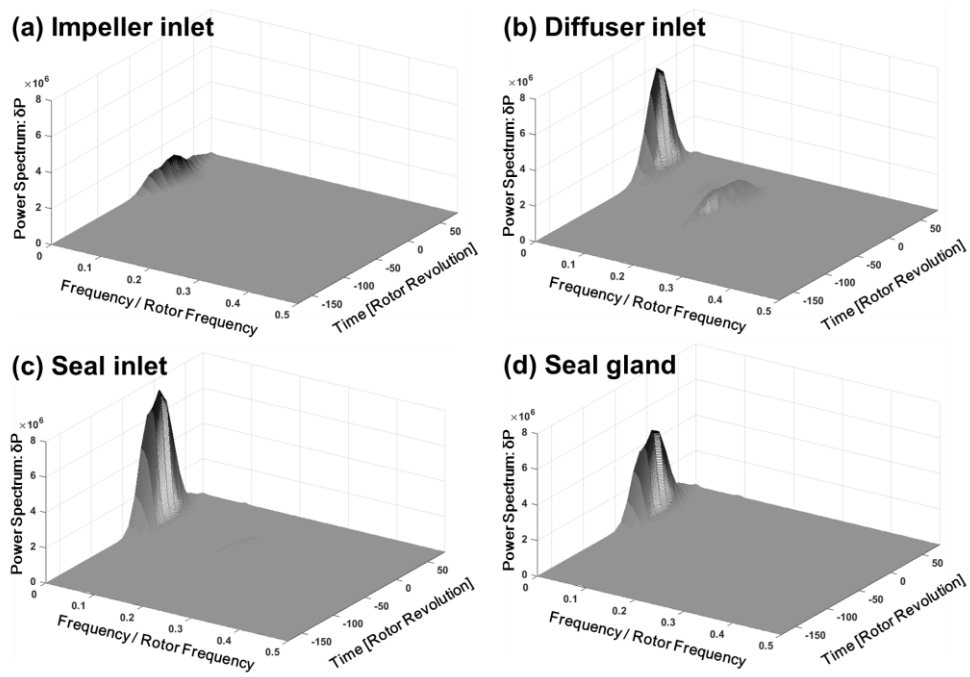

Figure 3.3. Spectrogram at each meridional position: (a) impeller inlet, (b) diffuser inlet, (c) seal inlet, (d) seal gland

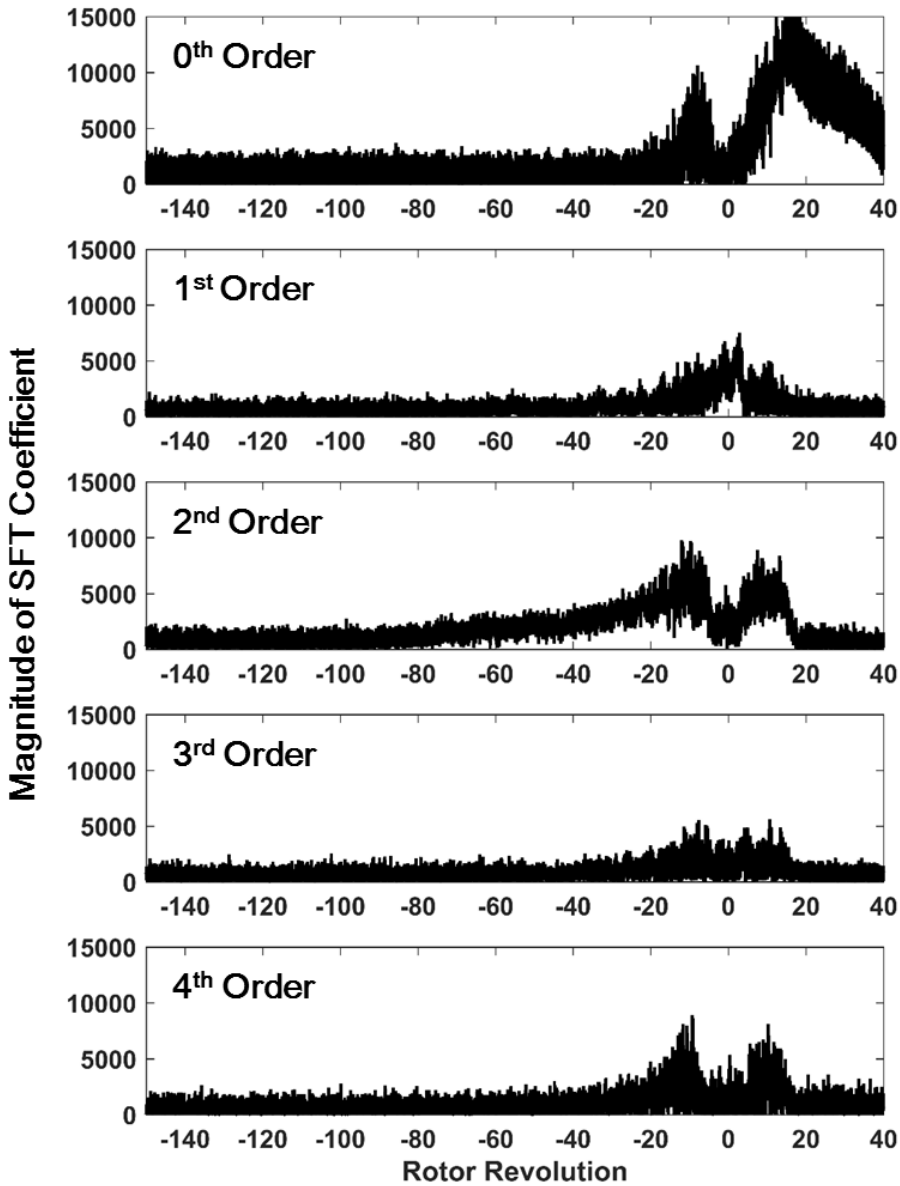

Figure 3.4. Magnitude of Spatial Fourier Transform coefficients at diffuser inlet

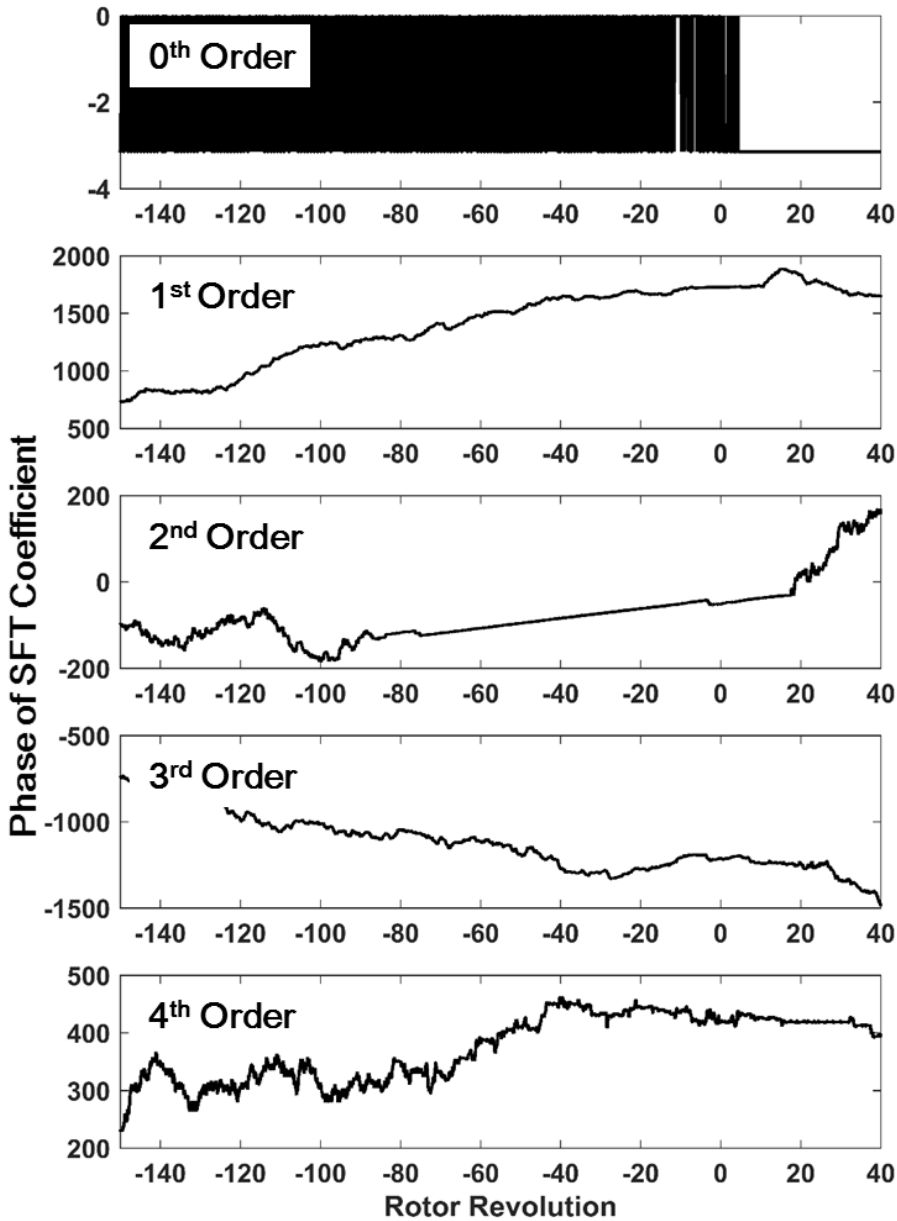

Figure 3.5. Phase of Spatial Fourier Transform coefficients at diffuser inlet

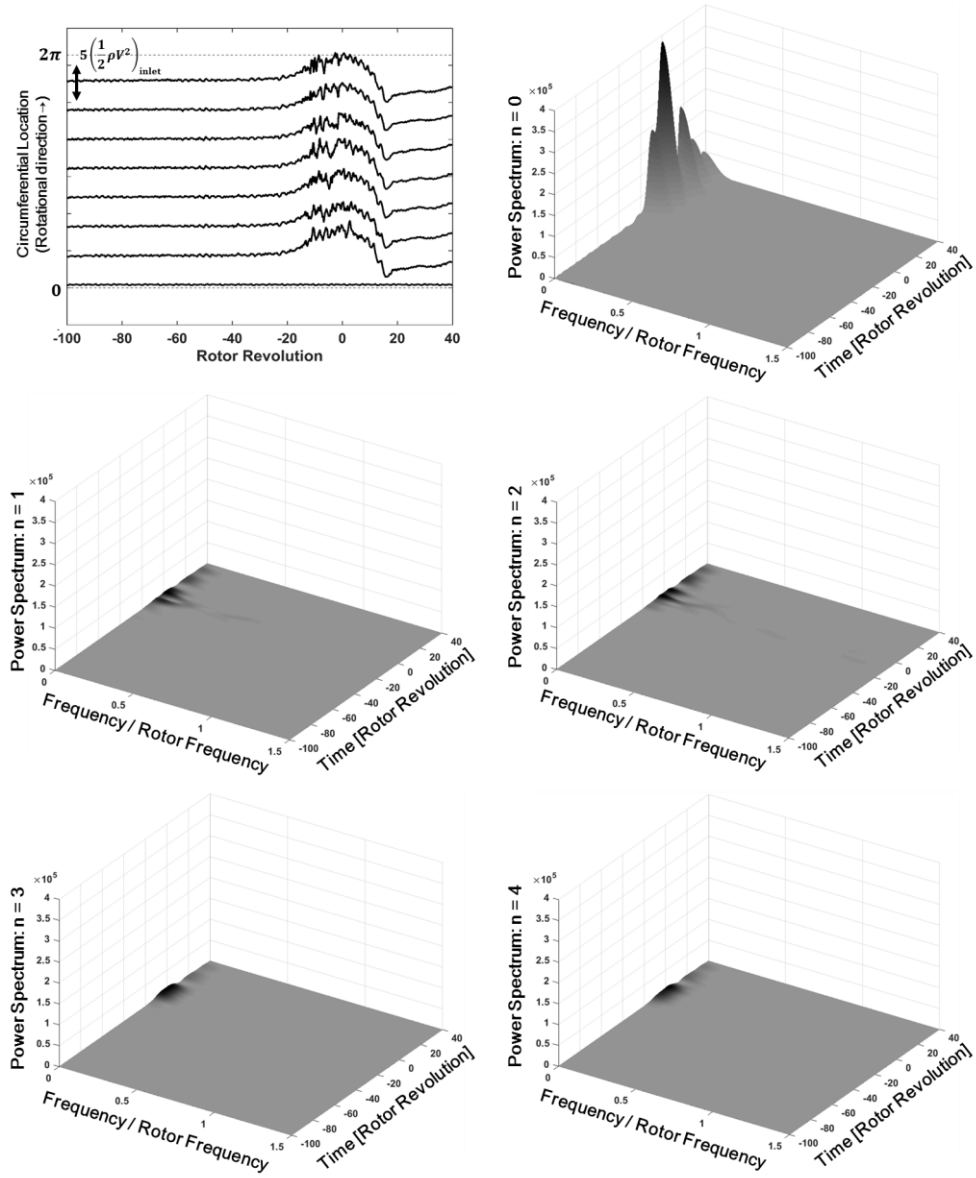

Figure 3.6. Impeller inlet Kulites: path-time graph and corresponding spectrograms of 0th, 1st, 2nd, 3rd, and 4th spatial Fourier coefficients.

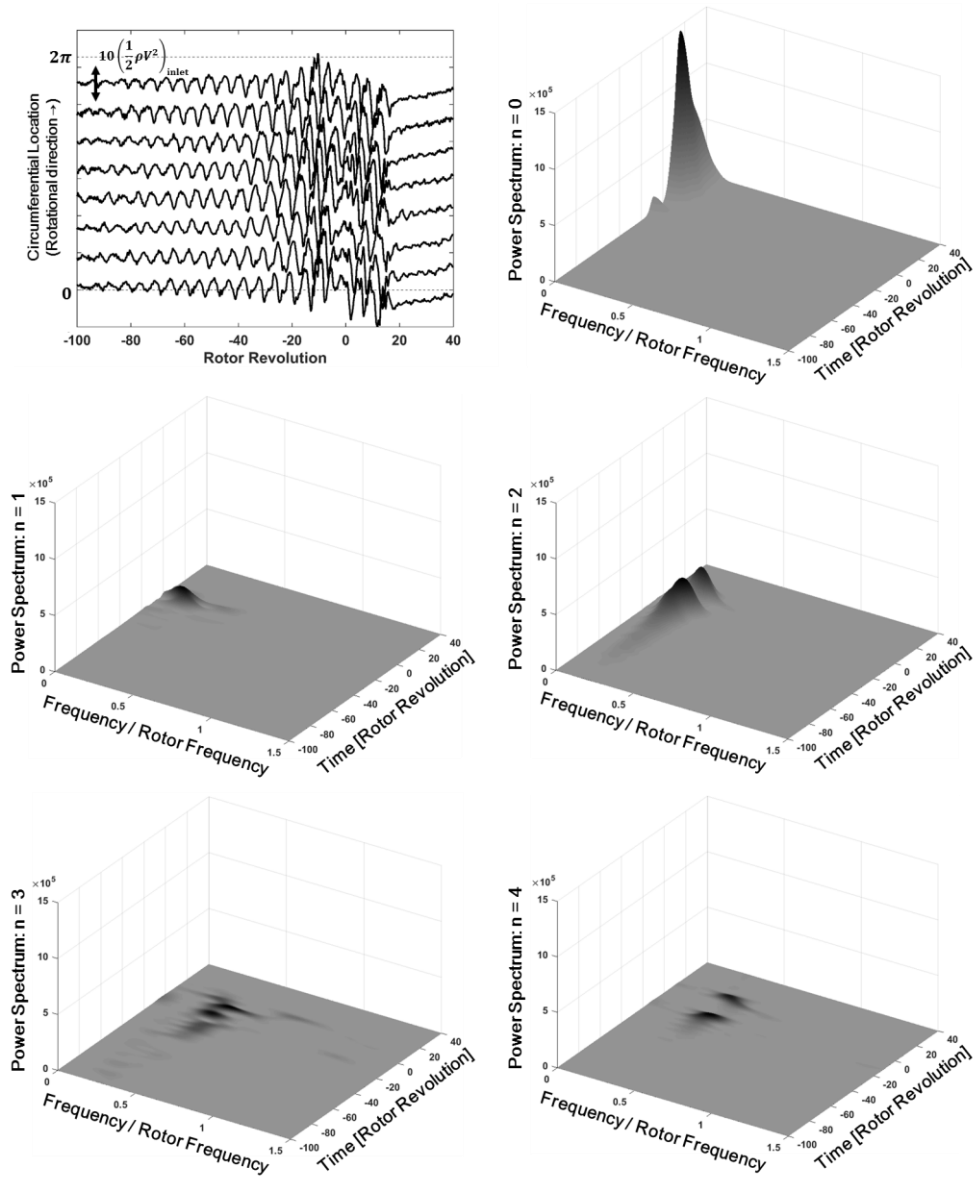

Figure 3.7. Diffuser inlet Kulites: path-time graph and corresponding spectrograms of 0th, 1st, 2nd, 3rd, and 4th spatial Fourier coefficients.

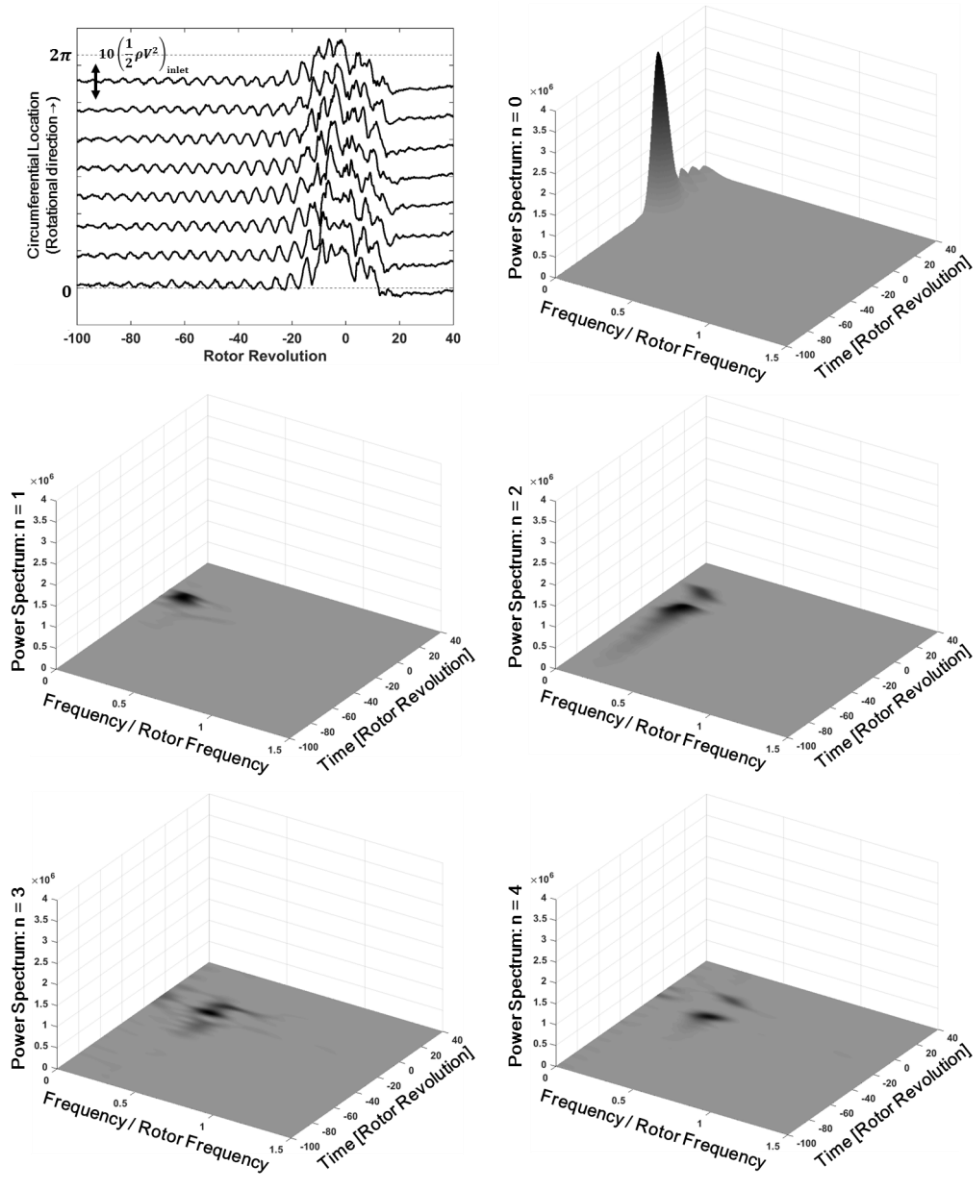

Figure 3.8. Seal inlet Kulites: path-time graph and corresponding spectrograms of 0th, 1st, 2nd, 3rd, and 4th spatial Fourier coefficients.

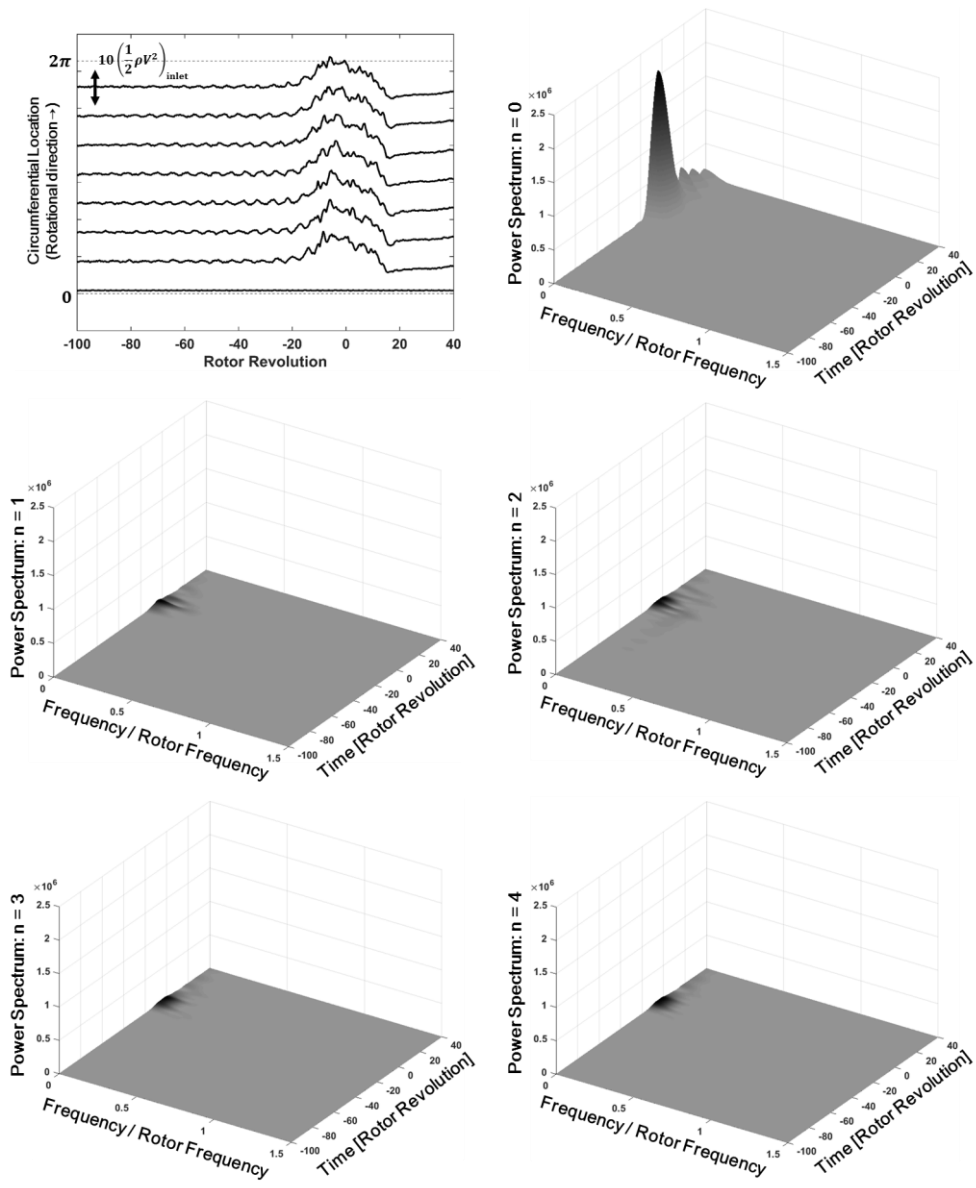

Figure 3.9. Seal gland Kulites: path-time graph and corresponding spectrograms of 0th, 1st, 2nd, 3rd, and 4th spatial Fourier coefficients.

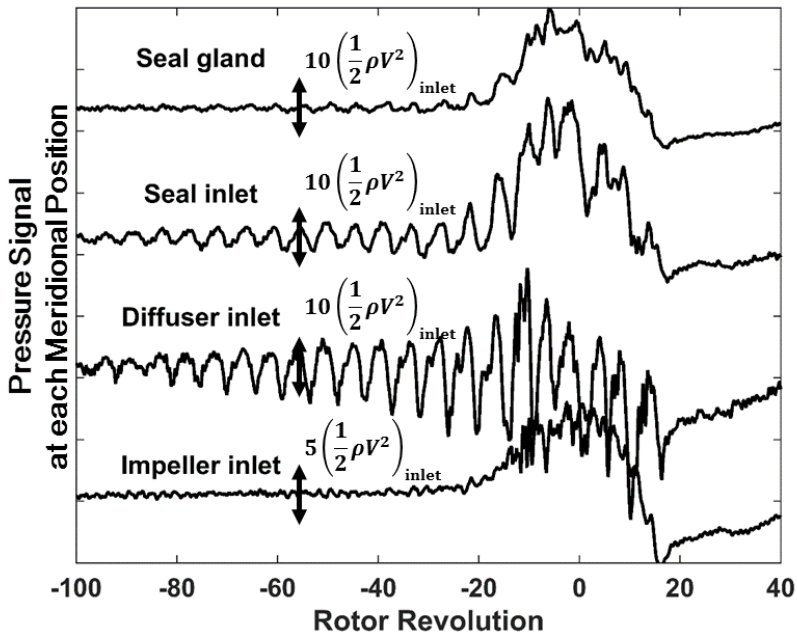

Figure 3.10. Pressure traces into surge at impeller inlet, at diffuser inlet, at seal inlet, and seal gland.

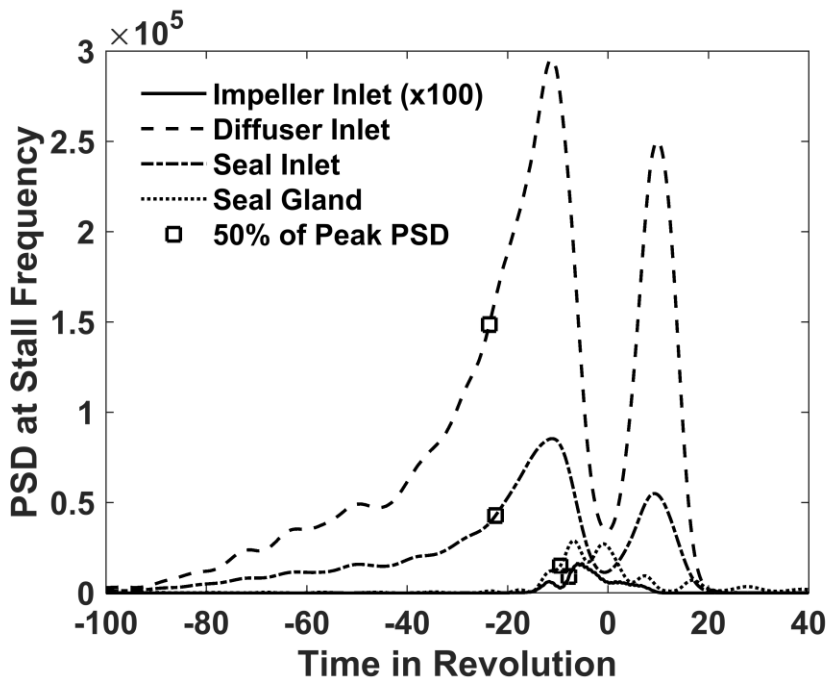

Figure 3.11. Traveling Wave Energy of the second harmonic at impeller inlet, at diffuser inlet, at seal inlet, and at seal gland

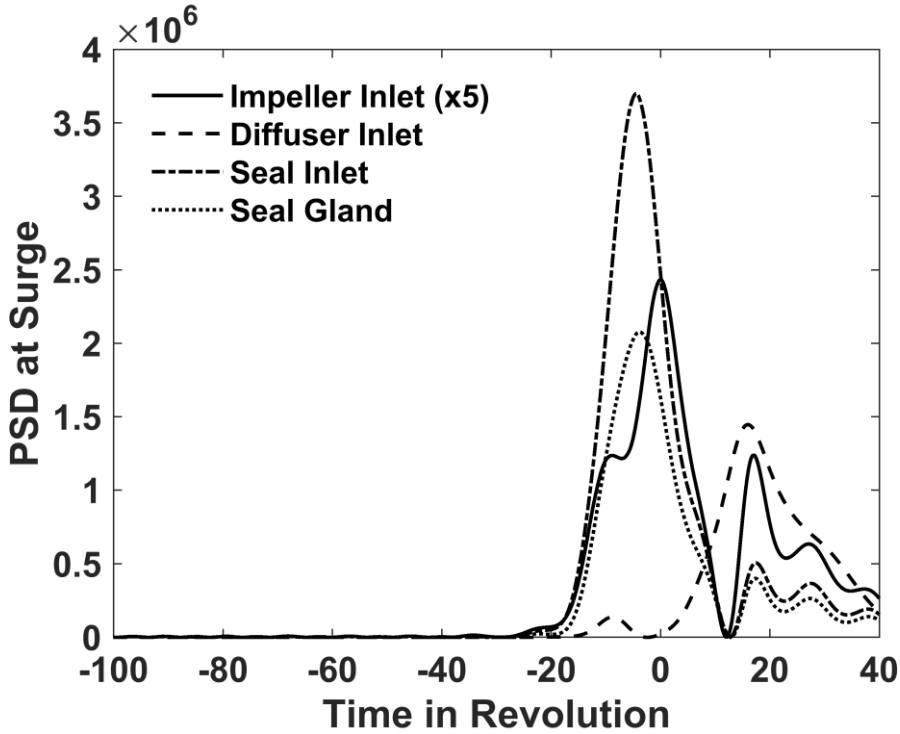

Figure 3.12. PSD magnitude of zeroth harmonic at zero frequency

Chapter 4. Eccentricity Effects on Stability

As discussed in the chapter 3, classic surge has been occurred in the compressor at concentric condition. During surge cycle, the modal type rotating stall has two stall cells and stall cells rotate at 0.19 times impeller frequency. In the chapter 4, the effects of eccentricity on performance and stability will be discussed. The objectives of the chapter 4 are follows.

(1) To compare compressor performance curve, which is pressure rise coefficient versus flow coefficient, against the level of eccentricity.

(2) To evaluate the effects of eccentricity on stability including

   A. the onset of rotating stall and surge;

   B. the number and the speed of rotating stall cells; and

   C. the unsteady behavior at inception.

4.1. Effects of Eccentricity on Steady Performance – Pressure Rise Coefficient

In the previous research, Graf et al. [11] reported that eccentricity exerts bad influences on pressure rise characteristic in an axial compressor. On the other hand, pressure rise in an axial compressor has not been influenced by eccentricity in the works of Young et al. [26]. Overall pressure rise characteristic of the shrouded centrifugal compressor in the research is plotted in the Figure 4.1. It can be seen

that eccentricity leads to degradation of pressure rise but the value is small. Figure 4.2 shows the effects of eccentricity on total-to-static pressure rise coefficient through the impeller and Figure 4.3 illustrates static-to-static pressure rise coefficient through the diffuser. Even though the scale of pressure rise coefficient in Figure 4.1 is same as the scale in Figure 4.2, definite degradation of pressure rise through the impeller can be seen. However, degradation of pressure rise through diffuser cannot be seen in Figure 4.3. Therefore, larger degradation through the impeller implicates that loss arises through the impeller.

Eldin [6] reported that eccentricity causes large averaged leakage through secondary passage even though nominal seal clearance remains constant. Therefore, one reason of degradation is that impeller works for larger mass flow as eccentricity increases even though total mass flow remains constant through the compressor. The other reason is assumed to be inlet flow distortion by distorted flow from secondary passage same as the result of Hynes [15].

4.2. Influence of Eccentricity on the Onset of Rotating Stall and Surge

Figure 4.4 describes the influence of eccentricity on the onset of rotating stall and surge. In the chapter 3, pre-stall events transitions to classic surge at the flow coefficient of 0.044 at the baseline. To find the onset of surge and rotating stall, procedure used in chapter 3 is adapted. The first eccentricity case, which is 19.6%

eccentricity, goes directly into classic surge at flow coefficient of 0.044 same as the baseline. On the other hand, the second eccentricity case, which is 26.2% eccentricity, has rotating stall at first at flow coefficient of 0.0448, then the compressor goes into classic surge at lower flow coefficient. At this eccentricity case, steady flow coefficient at the onset of surge cannot be unfortunately measured due to sudden stop of the compressor right after surge. The fourth case and the fifth case, which are 37.8% and 58.7% eccentricity, have also same trends of the onset of instability with 26.2% eccentricity. As a result, rotating stall occurs at higher flow coefficient as eccentricity increases but surge occurs at same flow coefficient. This sensitivity of the onset of surge and rotating stall has been caused because eccentricity leads to non-axisymmetric flow redistribution along secondary passage. Therefore, rotating stall as two-dimensional instability is only sensitive to eccentricity.

4.3. Unsteady Compressor Response against Eccentricity

At the baseline, rotating stall can be detected at -80 revolution before surge. Figure 4.5 through Figure 4.9 shows power spectrum of first four harmonic SFT coefficients at the inception of rotating stall and surge. As mentioned in section 4.2, some plots of Traveling Wave Energy of surge at 26.2% and 58.7% eccentricities are missing in figures. Figure 4.5 has very similar response with the baseline and the compressor directly goes into classic surge. On the other hand, Figure 4.6

through Figure 4.9 show that the compressor has the inception of rotating stall and surge at different flow coefficients. At all cases, modal type pre-stall precedes rotating stall and the mode of pre-stall is the combined mode of the second mode and the third mode. After rotating stall occurs, the third mode small disturbance still exists. When surge occurs, rotating stall has been going in and out during surge cycle at all eccentricity cases same as the baseline case. Figure 4.10 illustrates that the number of stall cells has not been affected by eccentricity. Figure 4.11 shows the frequency of stall cells at the stall inception. The rotating stall at the cases of 9.6% and 19.6% eccentricity have the similar frequency of 0.192 and 0.19 time rotor frequency. On the other hand, the rotating stall at the other cases have the frequency of 0.18 through 0.182 time rotor frequency. Therefore, the speed of rotating stall decreases when rotating stall precedes classic surge at higher flow coefficient.

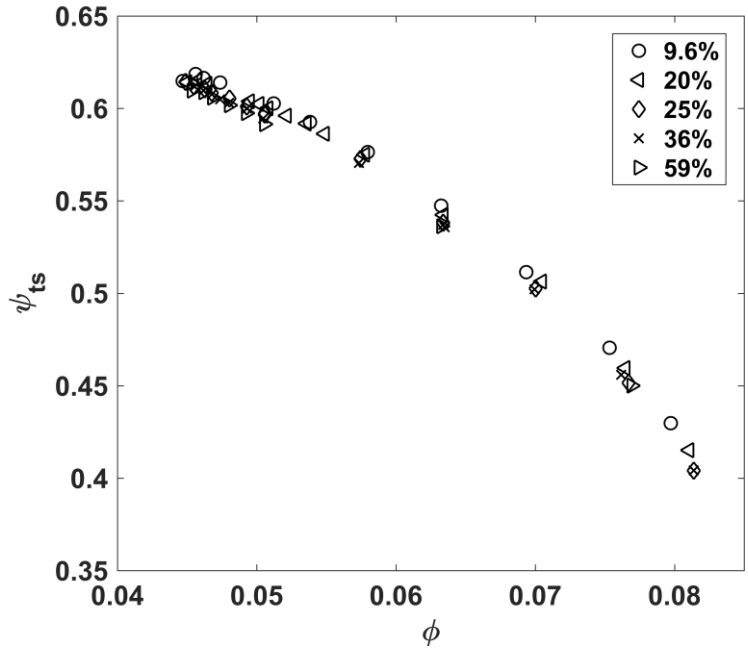

Figure 4.1. Overall total-to-static pressure rise coefficient vs. flow coefficient

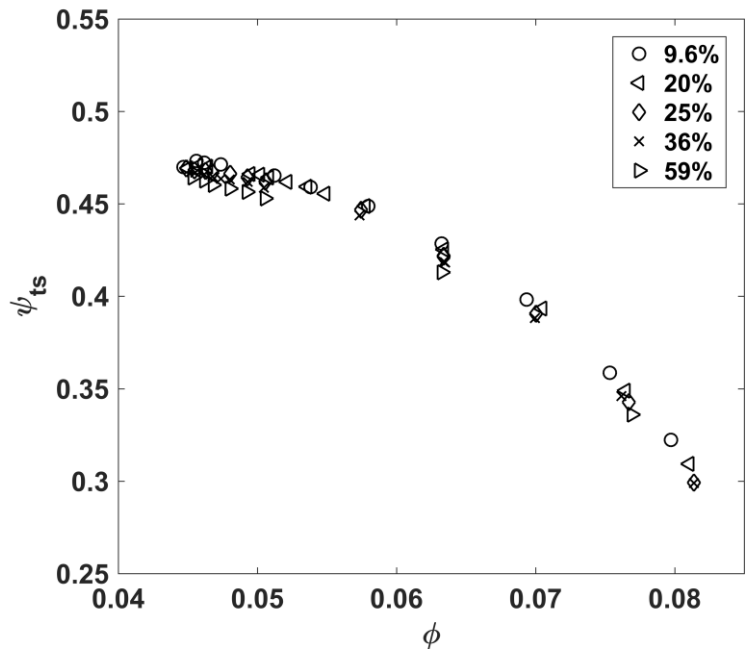

Figure 4.2. Impeller total-to-static pressure rise coefficient vs. flow coefficient

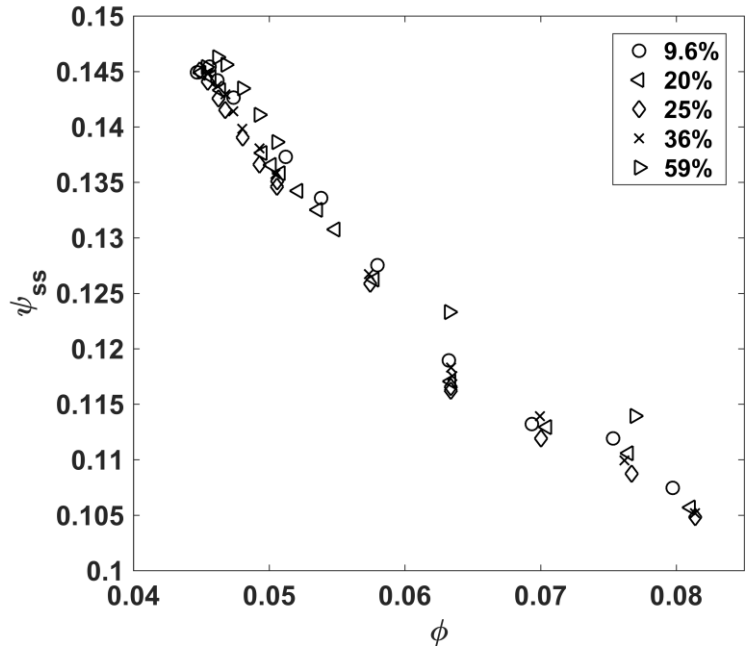

Figure 4.3. Diffuser static-to-static pressure rise coefficient vs. flow coefficient

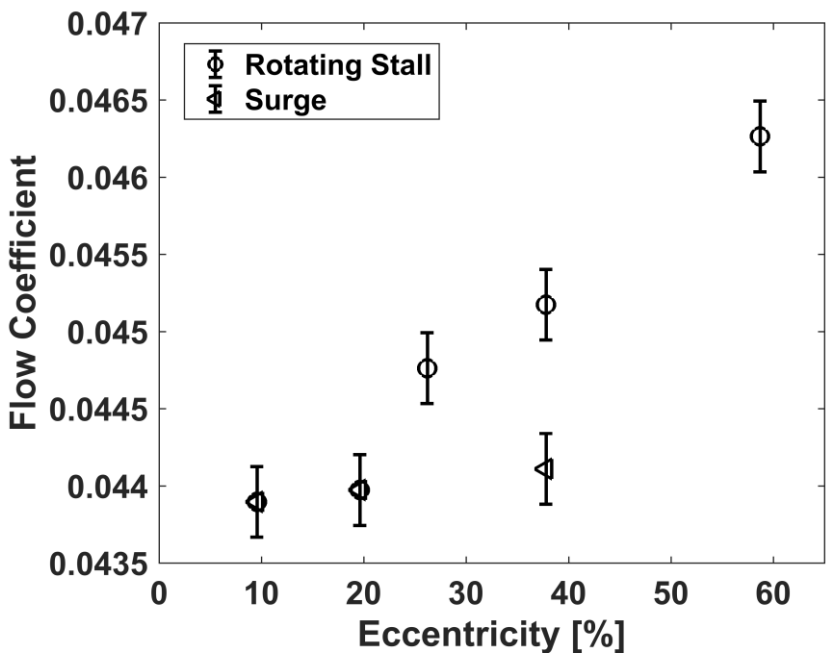

Figure 4.4. The onset of rotating stall and surge

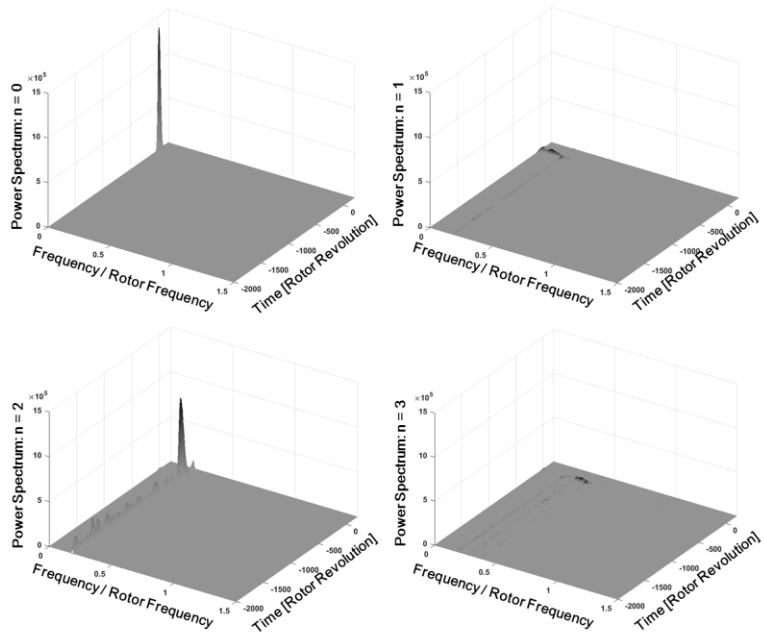

Figure 4.5. Case 2: Diffuser inlet Kulites: path-time graph and corresponding spectrograms of 0th, 1st, 2nd, and 3rd spatial Fourier coefficients. (Surge, $\phi = 0.0440,\ e = 19.6\%$)

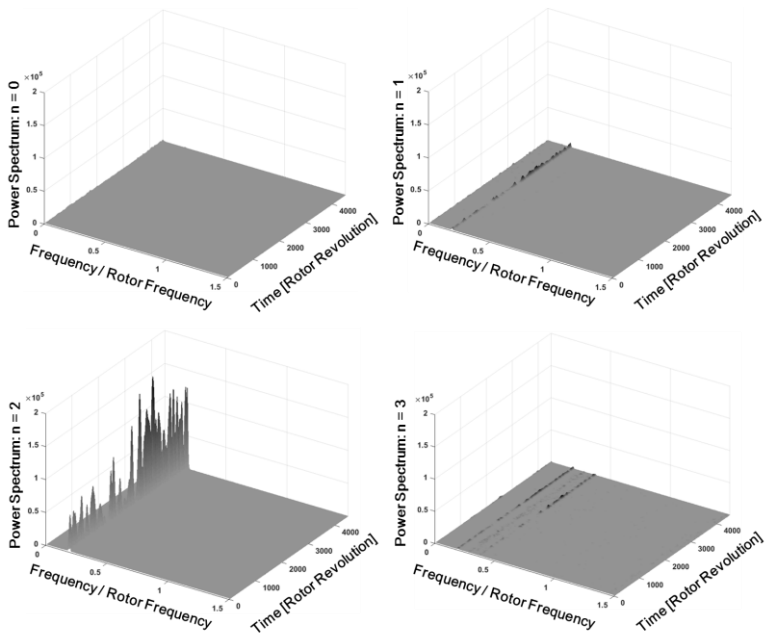

Figure 4.6. Case 3: Diffuser inlet Kulites: path-time graph and corresponding spectrograms of 0th, 1st, 2nd, and 3rd spatial Fourier coefficients. (Rotating stall, $\phi = 0.0448,\ e = 26.2\%$)

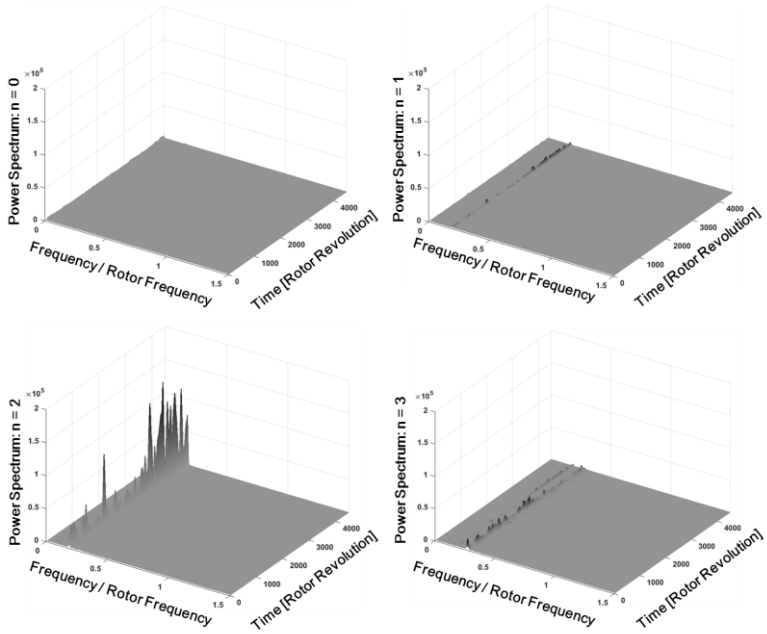

Figure 4.7. Case 4: Diffuser inlet Kulites: path-time graph and corresponding spectrograms of 0th, 1st, 2nd, and 3rd spatial Fourier coefficients. (Rotating stall, $\phi = 0.0452,\ e = 37.8\%$)

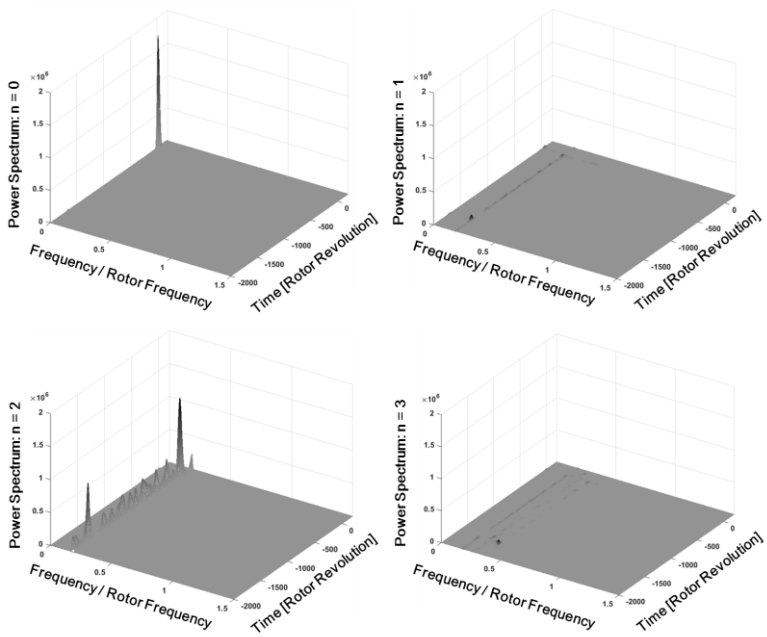

Figure 4.8. Case 4: Diffuser inlet Kulites: path-time graph and corresponding spectrograms of 0th, 1st, 2nd, and 3rd spatial Fourier coefficients. (Surge, $\phi = 0.0441,\ e = 37.8\%$)

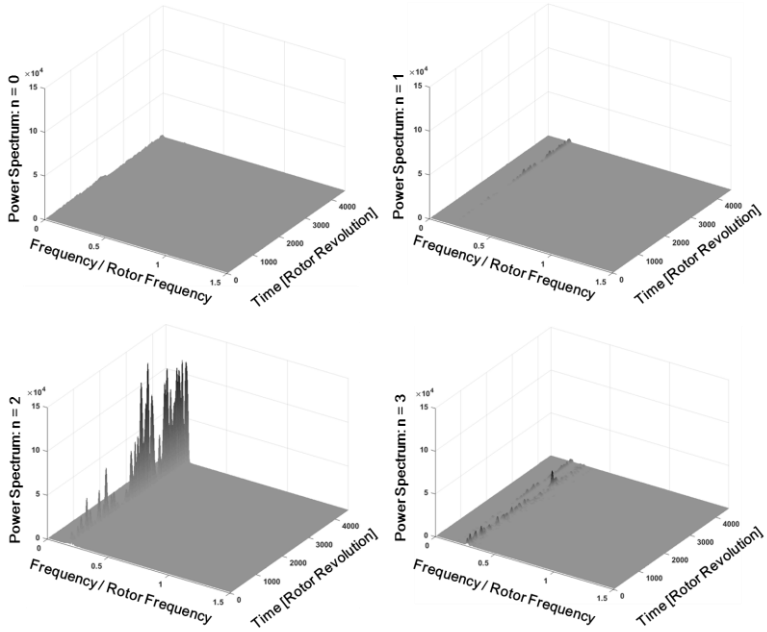

Figure 4.9. Case 5: Diffuser inlet Kulites: path-time graph and corresponding spectrograms of 0th, 1st, 2nd, and 3rd spatial Fourier coefficients. (Rotating stall, $\phi = 0.0463,\ e = 58.7\%$)

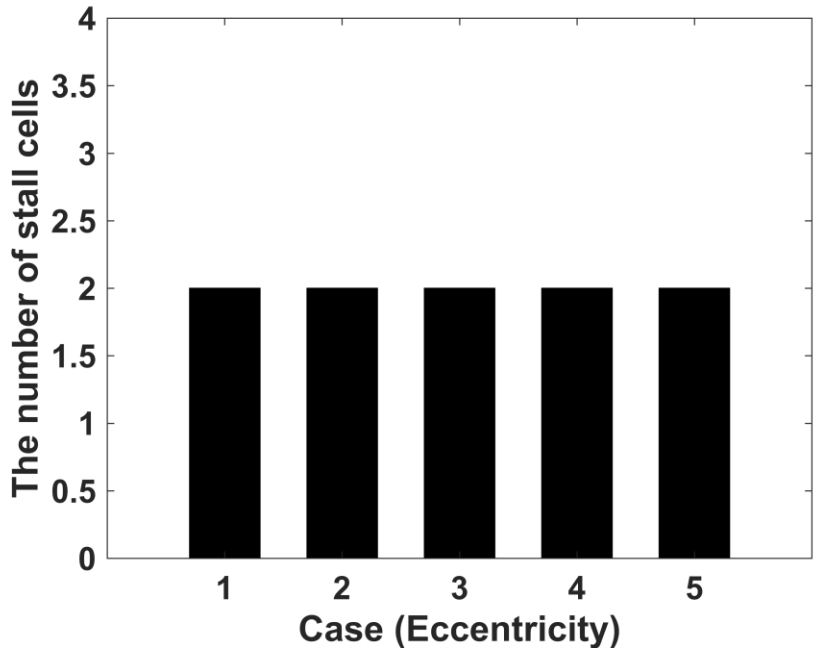

Figure 4.10. The number of stall cells against eccentricity

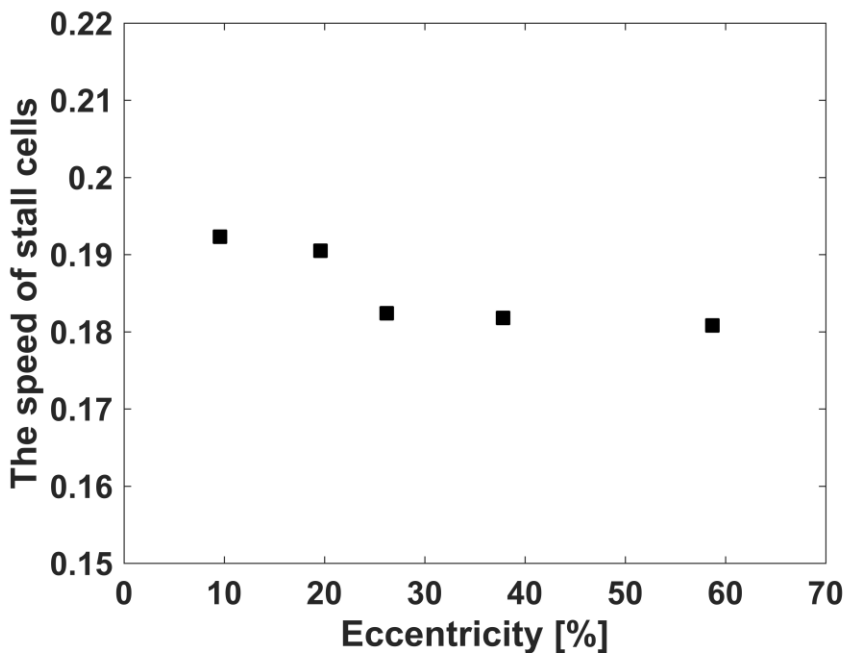

Figure 4.11. The frequency of rotating stall cells against eccentricity

Chapter 5. Conclusions

The effects of eccentricity on stability of a high-speed shrouded centrifugal compressor have been firstly measured. The research has investigated steady performance, the onset of instability, the behavior of instability against the level of eccentricity. The main conclusions of the research are as follows.

(1) The overall pressure rise coefficients have been little influenced by eccentricity.

(2) In the baseline case, the compressor directly goes into classic surge at the flow coefficient of 0.044. At this flow coefficient, the number of rotating stall cells is two and the frequency of stall cells is 0.19 times rotor frequency.

(3) The onset of rotating stall has been sensitive to eccentricity. Therefore, rotating stall arises at the flow coefficient of 0.0463 at 58.7% eccentricity.

(4) The onset of surge has been insensitive to eccentricity.

(5) The number of rotating stall cells has not been influenced by the level of eccentricity but the frequency of rotating stall decreases when the compressor suffers from only rotating stall at higher flow coefficient.

Bibliography

[1] Adbelhamid, A. N., 1980, “Analysis of Rotating Stall in Vaneless Diffusers of Centrifugal Compressors,” Proceedings of ASME Turbo Expo 1980, 80-GT-184, 1-8.

[2] Berdanier, R. A., Smith, N. R., Fabian, J. C., and Key, N. L., 2014, “Humidity Effects on Experimental Compressor Performance—Corrected Conditions for Real Gases,” Proceedings of ASME Turbo Expo 2014, GT2014-25790, 1-12.

[3] Cameron, J. D., and Morris, S. C., 2007, “Spatial Correlation Based Stall Inception Analysis,” Proceedings of ASME Turbo Expo 2007, GT2007-28268, 1-12.

[4] Cameron, J. D., Bennington, M. A., Ross, M. H., Morris, S. C., and Corke, T. C., 2007, “Effects of Steady Tip Clearance Asymmetry and Rotor Whirl on Stall Inception in an Axial Compressor,” Proceedings of ASME Turbo Expo 2007, GT2007-28278, 1-12.

[5] Day, I. J., 2015, “Stall, Surge and 75 Years of Research,” Proceedings of ASME Turbo Expo 2015, GT2015-44109, 1-22.

[6] Eldin, A. M. G., 2007, “Leakage and Rotordynamic Effects of Pocket Damper Seals and See-Through Labyrinth Seals,” Dissertation, Texas A&M University.

[7] Emmons, H. W., Pearson, C. F., and Grant, H. P., 1955, “Compressor Surge and Stall Propagation,” Transaction of ASME, 79, 455-459.

[8] Etchevers, O., 1992, “Evaluation of Rotating Stall Warning Schemes for Axial Compressors,” Thesis, Massachusetts Institute of Technology.

[9] Frigne, P., Braembussche, R. V., 1984, “A Theoretical Model for Rotating Stall in the Vaneless Diffuser of a Centrifugal Compressor,” Proceedings of ASME Turbo Expo 1984, 84-GT-204, 1-7.

[10] Gordon, K. A., 1999, “Three-dimensional Rotating Stall Inception and Effects of Rotating Tip Clearance Asymmetry in Axial Compressors,” Dissertation, Massachusetts Institute of Technology.

[11] Graf, M. B., Wong, T. S., Greitzer, E. M., Marble, F. E., and Tan, C. S., 1998, “Effects of Nonaxisymmetric Tip Clearance on Axial Compressor Performance and Stability,” Journal of Turbomachinery, 120(4), 648-661 (formerly ASME Paper 97-GT-406).

[12] Greitzer, E. M., 1976, “Surge and Rotating Stall in Axial Flow Compressors Part 1: Theoretical Compression System Model,” Journal of Engineering for Power, 98(2), 190-198.

[13] Greitzer, E. M., and Moore, F. K., 1986, “A Theory of Post-Stall Transients in Axial Compression Systems: Part 2 – Application,” Journal of Engineering for Gas Turbines and Power, 108, 231-239.

[14] Gysling, D. L., Greitzer, E. M., 1994, “Dynamic Control of Rotating Stall in Axial Flow Compressors using Aeromechanical Feedback,” Proceedings of ASME Turbo Expo 1994, 94-GT-292, 1-18.

[15] Hynes, T. P., Greitzer, E. M., 1987, “A Method for Assessing Effects of Circumferential Flow Distortion on Compressor Stability,” Journal of Turbomachinery, 109(3), 371-379.

[16] Inoue, M., Kuroumaru, M., Tanino, T., Yoshida, S., and Furukawa, M., 2001, “Comparative Studies on Short and Long Length-Scale Stall Cell Propagating in an Axial Compressor Rotor,” Journal of Turbomachinery, 123(3), 24-30.

[17] Kang, J. S., 2002, “Stall Inception in a Centrifugal Compressor,” Dissertation, Seoul National University.

[18] Marechale, R. M., Ji, M., and Cave, M., 2015, “Experimental and Numerical Investigation of Labyrinth Seal Clearance Impact on Centrifugal Impeller Performance,” Proceedings of ASME Turbo Expo 2015, GT2015-43778, 1-11.

[19] Moore, F. K., and Greitzer, E. M., 1986, “A Theory of Post-Stall Transients in Axial Compression Systems: Part 1 – Development of Equations,” Journal of Engineering for Gas Turbines and Power, 108, 68-76.

[20] Pullan, G., Young, A. M., Day, I. J., Greitzer, E. M., and Spakovszky, Z. S., 2015, “Origins and Structure of Spike-Type Rotating Stall,” Journal of Turbomachinery, 137(5), 051007-051007-11.

[21] Schleer, M. W., 2006, “Flow Structure and Stability of a Turbocharger Centrifugal Compressor,” Dissertation, Eidgenössische Technische Hochschule Zürich.

[22] Spakovszky, Z. S., 2001, “Applications of Axial and Radial Compressor Dynamic System Modeling,” Dissertation, Massachusetts Institute of Technology.

[23] Spakovszky, Z. S., Roduner, C. H., 2009, “Spike and Modal Stall Inception in an Advanced Turbocharger Centrifugal Compressor,” Journal of Turbomachinery, 131(3), 031012-1-031012-9.

[24] Tryfonidis, M., Etchevers, O., Paduano, J. D., Epstein, A. H., and Hendricks, G. J., 1995, “Prestall Behavior of Several High-Speed Compressors,” Journal of Turbomachinery, 117(1), 62-80.

[25] Young, A. M., Day, I., and Pullan, G., 2012, “Stall Warning by Blade Passing Signature Analysis,” Journal of Turbomachinery, 135(1), 011033-011033-10.

[26] Young, A. M., Cao, T., Day, I. J., and Longley, J. P., 2016, “Accounting for Eccentricity in Compressor Performance Predictions,” Proceedings of ASME Turbo Expo 2016, GT2016-56681, 1-11.

Appendix A. Calibration

A-1. Fast Response Pressure Sensors (Kulite sensors)

Two models of Kulite sensors have been used in the research. XCQ-062 sensors have the range of 0-5 psid and XCE-062 sensors have the range of 0-30 psid. Two models have been calibrated separately.

Calibration is categorized into static calibration and dynamic calibration. Static calibration does not include frequency response but dynamic calibration includes frequency response. In the research, Kulite sensors at seal inlet and seal gland have been installed at some distance from the surface. Therefore, dynamic response needs to be check for sensors at seal inlet and seal gland. All calibration procedure has been observed by the Kulite manual.

Calibration jig

Calibration jig has been designed to calibrate eight Kulite sensors simultaneously. Inlet of a calibration jig connects to a calibrator (Fluke PPC4E Pressure Controller/Calibrator for XCQ-062 and Mensor Calibrator). Outlet connects to a solenoid valve to purge. The chamber inside the calibration jig has flat surfaces for dynamic calibration. Holes for Kulites arranges at the same distance from centerline which meets the center of holes of inlet and outlet.

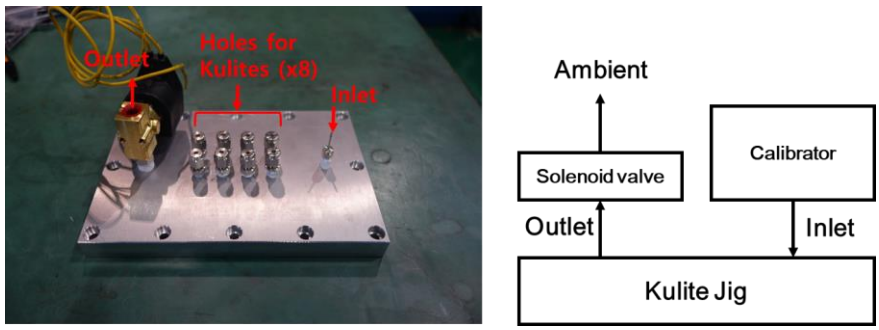

Figure A.1. Description of calibration jig

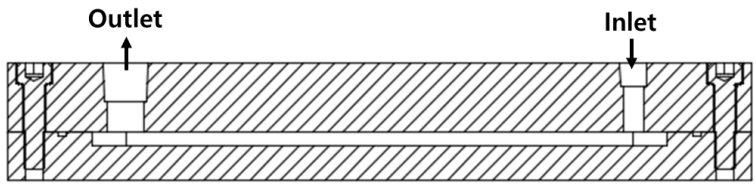

Figure A.2. Chamber inside the calibration jig

As described in chapter 2, Kulite sensors at seal inlet and seal gland have not been installed at the surface of a flow passage. Therefore, lagging or Helmholtz resonance might exit. To compensate these, each two sensor holes have different shapes and these shapes are same with the holes at seal inlet and seal gland.

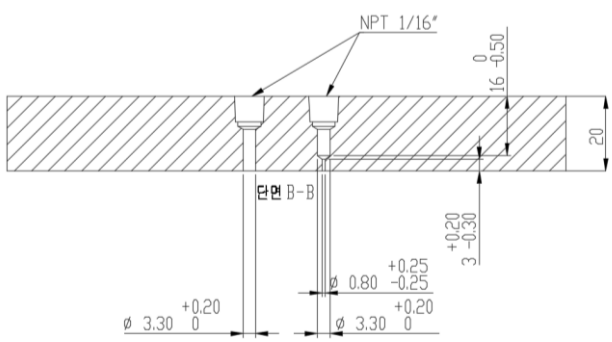

Figure A.3. Flush mounting and non-flush mounting

Static calibration

XCQ-062 sensors are calibrated at 11 points from -5 psi to 5 psi and XCE-062 sensors are calibrated at least 10 points from 0 psi to 30 psi. Totally thirty two Kulite sensors have been calibrated and one example of calibration data is shown in the Figure A.4 (a).

Dynamic calibration

Almost fast response pressure sensors are calibrated with statically when sensors are mounted at the same level of surfaces, which is called flush mounting. Unfortunately, some cases cannot be mount at the face of surfaces. Then, sensors might be installed with the other ways (Figure A.3). Therefore, dynamic calibration between flush mounting and non-flush mounting has to be needed.

The Helmholtz resonance frequency due to the non-flush mounting cavity is 13.6 kHz. Therefore, Helmholtz frequency is higher than frequency interest at seal inlet and seal gland in the research. To confirm time lag of data between flush mounting and non-flush mounting, the chamber has been pressurized up to 25 psi and the solenoid valve at outlet has been suddenly opened. This is called a step pressure generator. The sampling rate has been set to 204.8 kHz. The pressure traces are shown in the Figure A.4 (b). FFT result of the pressure traces is also shown in the Figure A.4 (c). In this calibration test, frequency ranges from 0 to 50 Hz during purge, unfortunately. Figure A.4 (d) is the result of dynamic calibration and the

peak locates at zero. Therefore, time lag of two signals between flush mounting and non-flush mounting can be treated as zero.

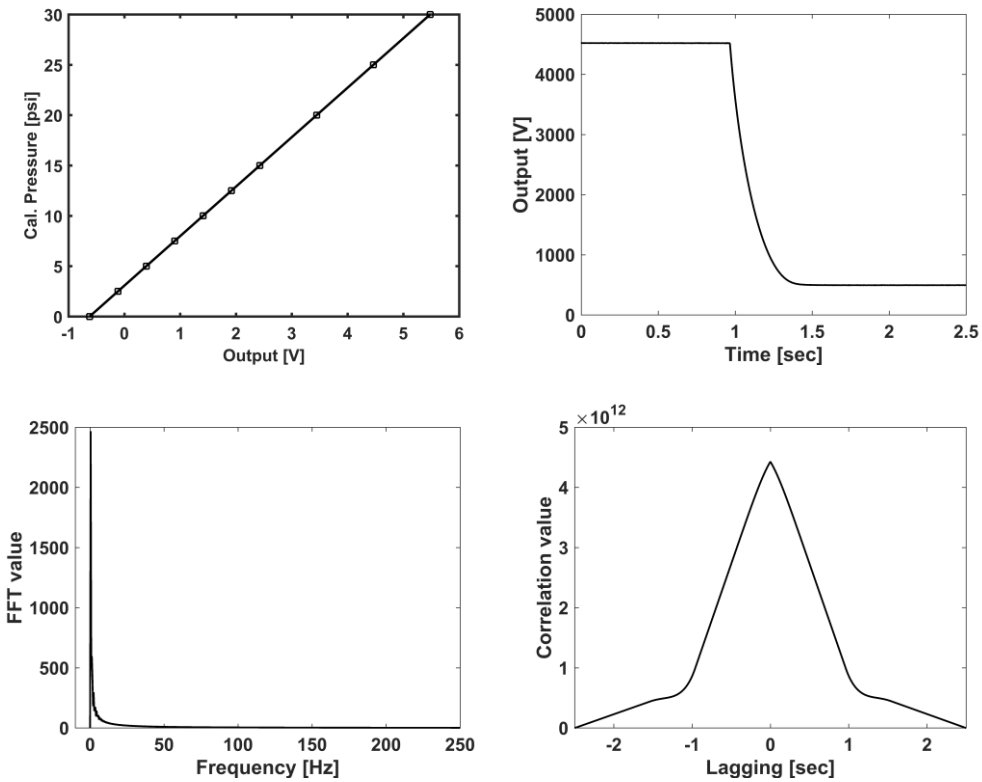

Figure A.4. The results of Kulite calibration (left-to-right order): (a) One example of Kulite calibration results, (b) Raw signal of Kulite sensor during purge, (c) FFT value of raw signal during purge, (d) Cross correlation of Kulite sensors located at same distance from inlet and outlet

Reference: Kulite, "Pressure Transducer Handbook"

(Link: https://www.kulite.com/technology/reference-library/

Latest link update in this thesis: July 14, 2017)

A-2. Gap sensor

The response of gap sensors are highly dependent on material of a counterpart. Therefore, calibration for material has to be needed. In this case, the sample, same material of the test impeller, has been attached to the calibrator (AEC-1008). The assembly of a gap sensor and a calibrator is shown in Figure A.5. The converter of gap sensors can adjust the slope, the offset, and the linearity. Therefore, gap sensors have been calibrated to have good linearity at the most interesting range in the research. The results of calibration and repeatability test are shown in Figure A.6.

Figure A.5. Calibration of gap sensors

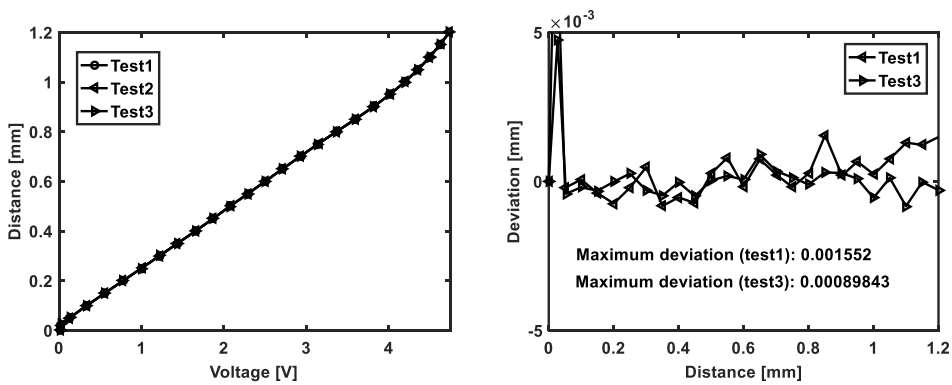

Figure A.6. Results of gap sensor calibration and repeatability check

요약문 (국문초록)

고속 슈라우드 원심압축기 안정성에 대한 편심 영향 측정

김수용

기계항공공학부

서울대학교 대학원

슈라우드 원심압축기에서 편심(eccentricity)은 임펠러와 케이싱 사이의 이차유로에 원주 방향의 불균일 유동을 야기한다. 편심에 의해 생긴 불균일 유동은 다시 슈라우드 원심압축기 입구에서 주유동과 섞이게 되며, 압축기 전체에 다시 원주방향 불균일 유동을 생성하여 높은 유량에서의 유동 불안정성을 야기할 수 있다. 편심 및 원주방향 불균일 유동장에 의한 불안정성 연구는 축류 압축기에서 꾸준히 진행되어 왔지만 슈라우드 원심압축기에서는 진행된 바가 없다. 따라서 본 연구에서는 고속 슈라우드 원심압축기 안정성에 대한 편심 영향을 실험적으로 측정하였다. 실험은 항공우주연구원에 위치한 터보차저 리그 설비를 사용하였으며, 압축기 임펠러와 케이싱을 재설계하여 편심 실험을 할 수 있도록 제작하였다. 유동 불안정성을 측정하기 위해 각 8개의 고속 응답 압력 센서 (fast response pressure transducer)를 원주방향으로 임펠러 입구, 디퓨저 입구, 라비린스 (labyrinth) 씰 입구

및 라비린스 씰 공동 (gland)에 각각 설치하였다. 실험은 9.6%의 편심량을 기준 케이스로 하여, 19.6%, 26.2%, 37.8% 및 58.7%의 편심량에 대해 슈라우드 원심압축기의 불안정성을 측정하였다. 실험결과는 다음과 같다. (1) 압축기 전체 압력 상승 계수 (pressure rise characteristic)은 편심 영향을 거의 받지 않았다. (2) 기준 케이스에서는 스톨과 서지가 동시에 일어나는 Classic surge가 흐름계수 (flow coefficient) 0.044에서 계측되었다. 이때 스톨셀의 개수는 2개며, 스톨 셀의 회전 주파수는 임펠러 회전 속도의 19%로 확인되었다. (3) 스톨 발달 흐름계수는 편심에 민감하게 반응하였으며, 스톨 발달 흐름계수는 58.7% 편심에서 0.0463까지 증가하였다. (4) 서지 발달 흐름계수는 편심에 의해 변하지 않았다. (5) 편심에 의해 스톨 셀의 개수는 변하지 않았지만, 스톨 셀의 회전 주파수는 편심이 커짐에 따라 작아졌다.

주 요 어 : 편심, 원심압축기, 슈라우드 임펠러, 안정성, 불안정성, 회전실속, 서지.

학 번 : 2015-22709